Journal of Materials Chemistry A

ROYAL SOCIETY OF CHEMISTRY

PERSPECTIVE

View Article Online
View Journal | View Issue

Check for updates

Cite this: J. Mater. Chem. A, 2026, 14, 284

Pressure-tuned 2D hybrid perovskites: emerging insights and future opportunities

Aditya Kutty [a] and Yang Song *[ab]

Two-dimensional (2D) hybrid organic–inorganic perovskites (HOIPs) are attracting growing attention for their exceptional structural flexibility, environmental stability, and unique quantum confinement effects. While chemical design has dominated the field, high-pressure techniques are emerging as a powerful, non-invasive route to tune lattice structures and optoelectronic responses *in situ*. Here, we present our perspective on the rapidly developing landscape of pressure-tuned 2D perovskites, focusing on Ruddlesden–Popper (RP) and Dion–Jacobson (DJ) systems. We highlight recent discoveries of pressure-induced structural phase transitions, direct–indirect bandgap conversions, broadband emission from self-trapped excitons, and the stabilization of metastable states. Particular emphasis is placed on contrasting soft *vs.* rigid organic spacers and lead-based *vs.* lead-free systems (Sn, Cu, Ge, and Bi). We argue that pressure not only serves as a diagnostic tool but also as a synthetic strategy for accessing hidden phases and functionalities. Looking ahead, the convergence of high-pressure spectroscopy, synchrotron techniques, and computational modeling offers exciting opportunities to rationally engineer sustainable, pressure-responsive optoelectronic materials.

Received 15th September 2025
Accepted 27th October 2025

DOI: 10.1039/d5ta07554h

rsc.li/materials-a

Open Access Article. Published on 28 Oktober 2025. Downloaded on 16.02.26 09:35:21.
This article is licensed under a Creative Commons Attribution-NonCommercial 3.0 Unported Licence.

[a]Department of Chemistry, University of Western Ontario, London, Ontario, N6A 5B7, Canada. E-mail: yang.song@uwo.ca

[b]Department of Physics and Astronomy, University of Western Ontario, London, Ontario, N6A 3K7, Canada

Aditya Kutty

Aditya Kutty is a PhD candidate in Chemistry at Western University, working with Prof. Yang Song on pressure-tuned structures and optoelectronic properties of 2D hybrid perovskites, emphasizing lead-free systems. He completed his MSc at Western (2024) and Honours BSc in Chemistry at the University of Toronto (2022). He is the first author of a 2025 Advanced Optical Materials paper on Dion–Jacobson 2D lead iodide perovskites and co-author of the Journal of Materials Chemistry C (2024 and 2025).

Yang Song

Yang Song is Professor of Chemistry at Western University in London, Ontario, Canada, cross-appointed in Physics & Astronomy. He earned a BSc from Peking University and a PhD from Iowa State University, followed by postdoctoral studies at Harvard University and the Carnegie Institution. His group develops and characterizes functional materials under extreme conditions using spectroscopy and synchrotron techniques, with emphasis on pressure-tuned structures and optoelectronic properties of 2D hybrid perovskites. He has authored over 100 publications, serves as Subject Editor of FACETS and on the Scientific Reports editorial board, and received the Ontario Early Researcher and Petro-Canada Young Innovator Awards.

This journal is © The Royal Society of Chemistry 2026

Open Access Article. Published on 28 Oktober 2025. Downloaded on 16.02.26 09:35:21.
This article is licensed under a Creative Commons Attribution-NonCommercial 3.0 Unported Licence.

1. Why pressure matters for 2D perovskites

Over the years, the application of halide perovskites in the field of optoelectronics has increased substantially owing to significant improvement of their photovoltaic performance.[1] As such, perovskites have garnered high interest in a number of optoelectronic applications, with the most prominent to date being solar cells.[2–4] Halide perovskites typically exist in either the three-dimensional (3D) or two-dimensional (2D) form, with 3D halide perovskites adopting an ABX_3 structure (where A is a small monovalent cation such as MA^+ or Cs^+, B is Pb^{2+} or Sn^{2+}, and X is a halide).[5,6] 3D perovskites have been shown to exhibit excellent light absorption,[7,8] long charge-carrier diffusion lengths,[9,10] and high defect tolerance.[11] However, 3D perovskites suffer from limited stability, restricted chemical composition, sensitivity to moisture and light, and the use of highly volatile and toxic cations.[12,13] To address these limitations, low-dimensional (especially 2D) perovskites have been explored.[6,13–15]

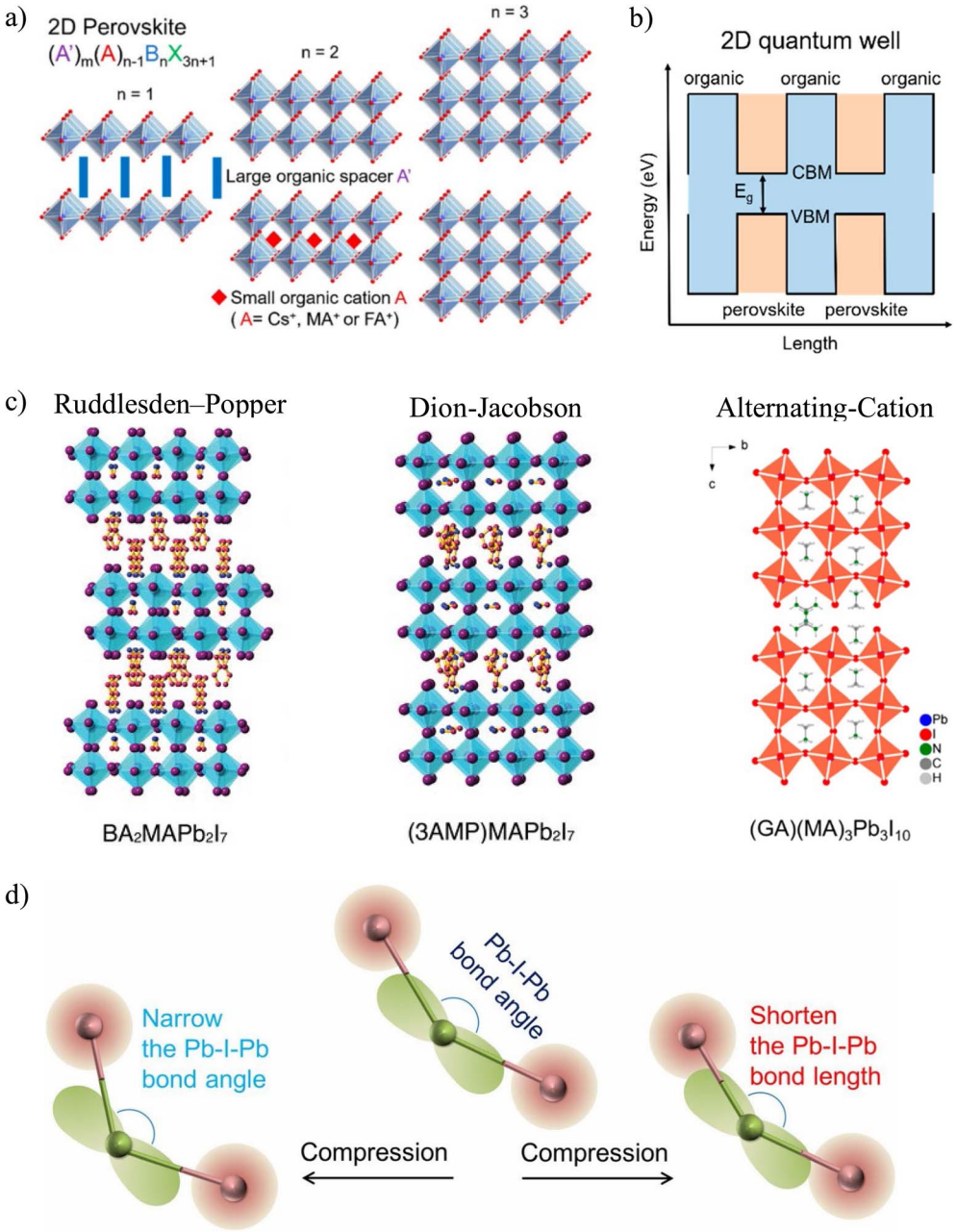

Fig. 1 Structure of 2D HOIPs. (a) Crystal structure for $n = 1$, 2, and 3 and (b) electronic structure showing 2D multiple quantum wells. Reproduced from ref. 6 with permission from American Chemical Society, copyright 2018. (c) RP and DJ phases, reproduced from ref. 13 with permission from Wiley-VCH GmbH, copyright 2019, and alternating cation 2D HOIP crystal structures. Reproduced from ref. 6 with permission from American Chemical Society, copyright 2018. (d) Effect of external pressure on the Pb–I–Pb bond angle and Pb–I bond length. Reproduced from ref. 47 with permission from PNAS, copyright 2018.

Open Access Article. Published on 28 Oktober 2025. Downloaded on 16.02.26 09:35:21.
This article is licensed under a Creative Commons Attribution-NonCommercial 3.0 Unported Licence.

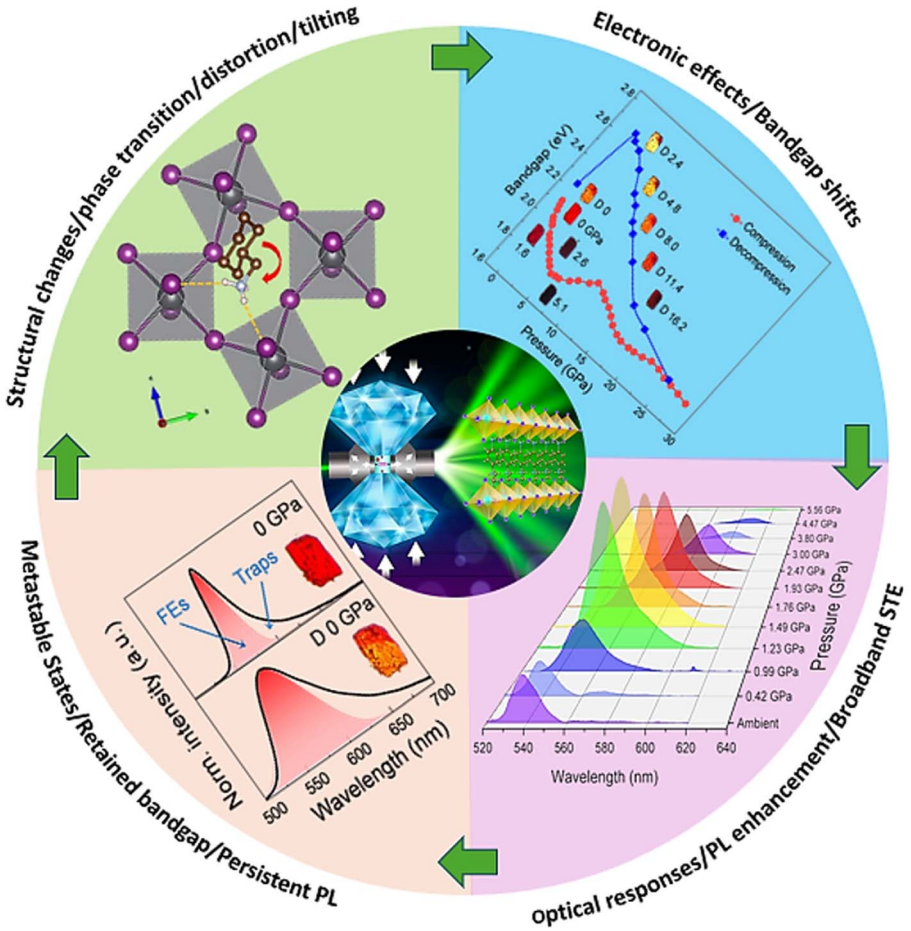

Fig. 2 Schematic roadmap of pressure effects in 2D hybrid perovskites. At the center, the diamond anvil cell (DAC) symbolizes pressure as an external tuning knob. Sequential arrows highlight the cascade of responses under compression: (i) structural changes such as phase transitions, octahedral tilting, and eventual amorphization; reproduced from ref. 36 with permission from American Chemical Society, copyright 2023. (ii) Electronic effects including bandgap narrowing, anomalous widening, and direct–indirect conversions; reproduced from ref. 53 with permission from Wiley-VCH GmbH, copyright 2020. (iii) Optical responses ranging from photoluminescence enhancement to broadband self-trapped exciton (STE) emission; reproduced from ref. 45 with permission from Wiley-VCH GmbH, copyright 2025. (iv) Metastable states where narrowed gaps or persistent PL remain after decompression. Reproduced from ref. 53 with permission from Wiley-VCH GmbH, copyright 2020. Together, these links illustrate how pressure serves not only as a probe but also as a design pathway for uncovering and stabilizing functional states in 2D perovskites.

In comparison to 3D perovskites, 2D perovskites exhibit greater stability towards humidity and light, and they tend to use bigger, less volatile organic cations (typically hydrophobic) which enhances both the thermal and chemical stability.[13] In general, 2D hybrid organic–inorganic perovskites (HOIPs) adopt the following formula $(A')_mA_{n-1}B_nX_{3n+1}$ (Fig. 1a), where A' is the organic spacer cation and can be either monovalent ($m = 2$) or divalent ($m = 1$) and n (or thickness) is the number of metal-halide octahedra between the adjacent organic layers.[6,13,16] The specific arrangement of the organic-inorganic layers forms a 2D multiple quantum well (MQW) electronic structure (Fig. 1b) with the organic spacers acting as insulating barriers, thus restricting the charge carriers in two dimensions.[6] This structure introduces both quantum and dielectric confinement effects, due to the difference in permittivity between the ionic perovskite layer and bulky organic cation,[17] while the organic layers provide environmental shielding, enhancing moisture resistance, and thermal stability.[6] Depending on the structure of the organic spacer, 2D perovskites can adopt Ruddlesden–Popper (RP, typically monovalent spacers) (Fig. 1c), Dion–Jacobson (DJ, typically divalent spacers) (Fig. 1c), or alternating-cation layered perovskite phases (ACI) (Fig. 1c).[6,13,18] RP phases contain metal-halide inorganic layers separated by bilayers of bulky ammonium spacer cations *via* weak van der Waals interactions,[13] allowing for greater interlayer distances and isolated layers exhibiting no perovskite–perovskite interactions,[6] while adopting a $(A')_2(A)_{n-1}B_nX_{3n+1}$ formula.[16] In contrast, DJ phases contain inorganic layers which stack directly on top of each other and employ bifunctional spacer cations, allowing direct bonding between layers,[13] and the close proximity of the layers enables weak perovskite–perovskite interactions,[6] while adopting a $(A')(A)_{n-1}B_nX_{3n+1}$ formula.[18] The ACI phase, a subclass of the DJ phase, employs alternating organic cations, typically guanidinium (GA) and methylammonium (MA), in the interlayer space, thus stabilizing the structure and adopting a $(A')_2(A)_nB_nX_{3n+1}$ formula.[13] In recent years, significant efforts

This journal is © The Royal Society of Chemistry 2026

Open Access Article. Published on 28 Oktober 2025. Downloaded on 16.02.26 09:35:21.
This article is licensed under a Creative Commons Attribution-NonCommercial 3.0 Unported Licence.

have gone into understanding and tuning the optoelectronic behavior of 2D perovskites, in particular through physical approaches. Most notably, high pressure has emerged as a powerful tool to continuously modulate both the structures and optoelectronic properties of 2D metal-halide perovskites without altering their composition.[19–46]

High pressure can impart changes to the structures of 2D perovskites resulting in distortion of the crystal lattice, depending on the direction of the applied external pressure, and subsequent octahedral tilting, bond contraction, and bond angle shortening,[6] whilst the earliest known account of pressure-induced octahedral tilting and bond contraction of 2D perovskites was on $(EA)_2CuCl_4$ in 1994.[48] In halide perovskites, compression results in relaxation of the inorganic lattice that occurs through bond contraction and octahedral tilting, with the former typically dominating at low pressures ($\leq\sim$2–3 GPa), while the latter tends to dominate at moderate to high pressure ($\sim$3–8 GPa).[49] Such structural changes are often governed by changes in the Pb–X–Pb bond angles and Pb–X bond lengths, such as in lead-iodide 2D perovskites where these changes result from narrowing of the Pb–I–Pb bond angle and shortening of the Pb–I bond length.[47] Structural changes subsequently result in changes to the optoelectronic properties with narrowing of the Pb–I–Pb bond angle leading to bandgap widening, whilst shortening of the Pb–I bond length leads to bandgap narrowing, as seen in Fig. 1d.[47] Such changes can reduce interlayer spacing and, in some cases, trigger irreversible structural rearrangements or amorphization. The onset of these transitions is typically lower in 2D HOIPs compared to their 3D counterparts, due to greater structural softness. For more complicated 2D HOIP structures especially those with $n > 1$, the intralayer and interlayer organic structures and their interplay with Pb–I octahedra need to be considered to understand the structure-optoelectronic property relationship.[39] High-pressure studies are particularly attractive because they not only allow for the modification of both the structures and optoelectronic properties but can also reveal rare pressure-induced phenomena.[47,50–56] In particular, high pressure has been shown to induce direct-to-indirect bandgap shifts,[51] broadband emission from self-trapped excitons,[52,55,56] hidden polymorphs,[47,55,56] the presence of metastable phases with enhanced properties,[47,50,53] and pressure-induced metallization in perovskite compositions.[54] In recent years several reviews have begun to map out the broader landscape of pressure tuning in perovskite materials.[57–59] However, no dedicated review has yet focused exclusively on 2D perovskites, in particular comparing RP and DJ types or systematically exploring the behavior of lead-based and lead-free systems under pressure. Our work aims to fill that gap by offering a detailed synthesis of high-pressure behavior in 2D perovskites, focusing on structural transitions, bandgap evolution, and the relationship between mechanical stress and optoelectronic properties. A roadmap schematic of pressure effects on 2D HOIPs is shown in Fig. 2.

We begin by classifying the structural motifs of 2D perovskites and then introduce the experimental tools and techniques used in high-pressure research (Section 2). Subsequent sections detail pressure-induced structural phase transitions of both RP and DJ systems (Section 3) and evolution of optical and electronic properties of RP and DJ systems (Section 4). We also highlight the growing interest in lead-free 2D perovskites (Section 5) and conclude with a forward-looking outlook (Section 6).

2. How we study 2D perovskites under pressure

Diamond, being the hardest natural material on earth, is capable of withstanding very high pressures and exhibits excellent transparency to both visible light and X-rays, thus making the diamond anvil cell (DAC) the optimal tool for performing *in situ* high pressure measurements.[60,61] For 2D perovskites, single-crystal and polycrystalline samples are compressed between the culets of opposing diamonds, often with a ruby chip (Cr^{3+} doped Al_2O_3, Al_2O_3: Cr^{3+}) for pressure calibration (*via* fluorescence shift) and a pressure-transmitting medium (*e.g.*, silicone oil and inert gases such as He, Ne, or Ar, and N_2) to maintain hydrostatic or quasi-hydrostatic conditions.[60,62] A schematic of a typical DAC can be seen in Fig. 3a. In terms of experimental methods, pressure-induced phase transitions and unit cell evolution are often revealed using synchrotron X-ray diffraction (XRD) with Raman and infrared spectroscopy (FTIR) able to provide further confirmation of the phase transitions along with pressure-induced changes in organic cation vibrations, octahedral tilting, and lattice strain.[36,45] The typical Raman and IR setup can be seen in Fig. 3b and c. *In situ* optical absorption (UV-vis) and photoluminescence (PL) spectroscopy track bandgap modulation and excitonic responses upon compression,[36,45] while time resolved photoluminescence (TRPL) can be used to examine charge carrier lifetimes.[21,34] A general setup for PL and UV-vis can be seen in Fig. 3d. In addition to experimental studies, computational studies, typically through density functional theory (DFT) calculations, can provide further confirmation of the pressure-induced changes to both the structures and optoelectronic properties.[36,37,45] However, this review will focus on experimental high-pressure effects. Recent improvements in high-pressure experimental platforms have enabled more precise control over pressure conditions and enhanced optical accessibility within diamond anvil cells, allowing for real-time, multimodal measurements. These advancements facilitate a deeper understanding of the correlation between structural changes and optoelectronic properties, ultimately guiding the rational design of pressure-tunable 2D perovskite materials.

3. Pressure-induced phase transitions in 2D perovskites

The layered nature of 2D hybrid organic–inorganic perovskites (HOIPs) gives rise to complex and highly tunable structural responses under hydrostatic pressure. Compared to their 3D counterparts, 2D HOIPs exhibit more diverse and pressure-accessible polymorphic behavior due to their soft organic interlayers and relatively weak van der Waals bonding.[6,13] This section summarizes representative high-pressure phase

Open Access Article. Published on 28 Oktober 2025. Downloaded on 16.02.26 09:35:21.
This article is licensed under a Creative Commons Attribution-NonCommercial 3.0 Unported Licence.

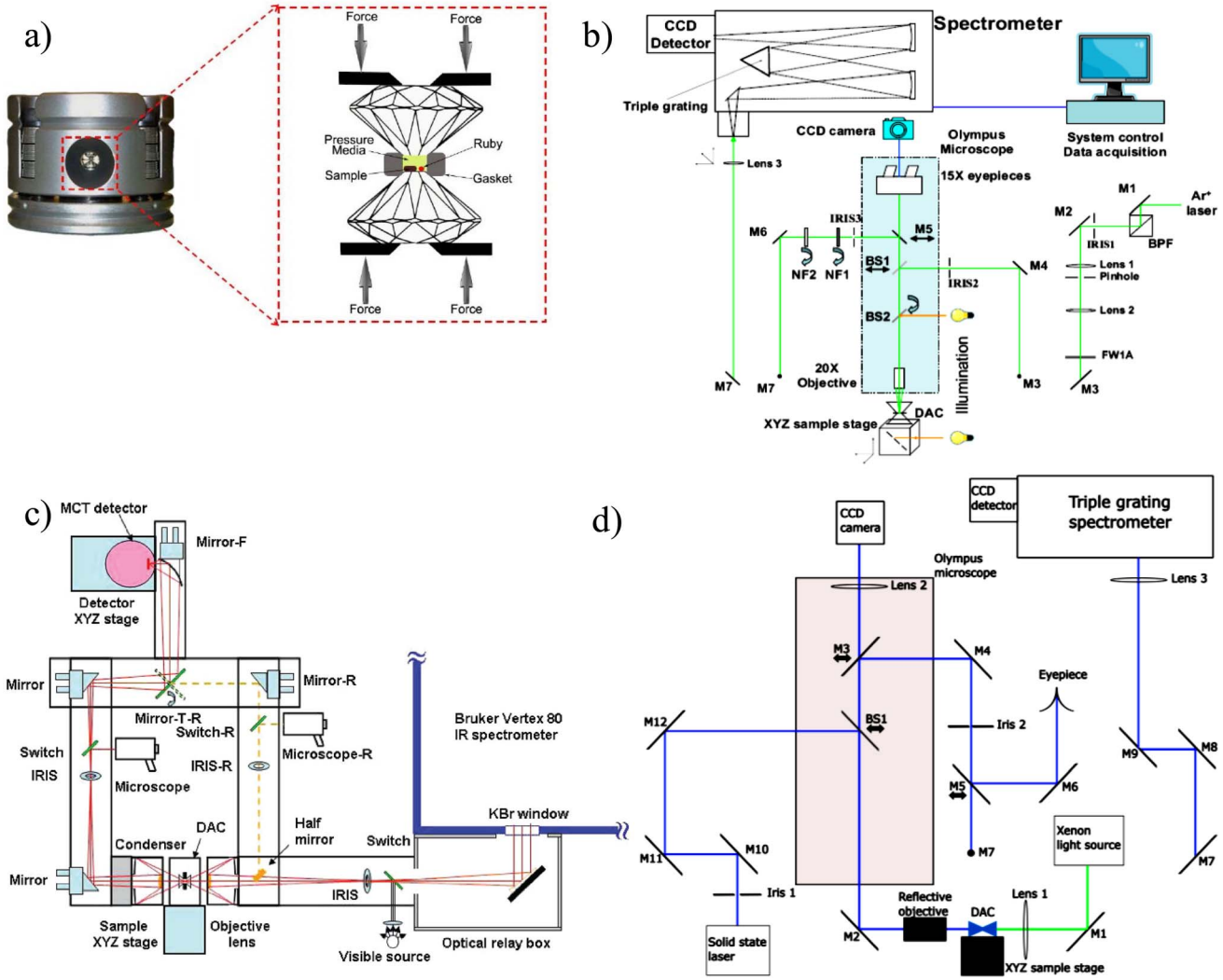

Fig. 3 High-pressure setup and instrumentation. (a) Schematic of a DAC. Reproduced from ref. 63 with permission from IntechOpen, copyright 2011. (b) Raman setup. Reproduced from ref. 64 with permission from the University of Western Ontario, copyright 2012. (c) FTIR setup. Reproduced from ref. 65 with permission from American Chemical Society, copyright 2010. (d) PL and UV-vis setup. Reproduced from ref. 66 with permission from the University of Western Ontario, copyright 2022.

transitions in selected 2D HOIPs, emphasizing how such transitions differ in RP and DJ-type systems and how spacer flexibility can influence phase stability and transformation pathways and how the type of spacer can also lead to the occurrence of rare phenomena such as negative linear compressibility (NLC) and decreased octahedral distortion.

3.1. RP-type 2D perovskites

Pressure-induced phase transitions have been observed at low pressures (typically <5 GPa) in most RP-type 2D HOIPs. For example, $(BA)_2PbI_4$ (BA = butylammonium), because of the soft organic spacers and van der Waals gaps, undergoes rapid and sequential structural phase transitions from its orthorhombic *Pbca* phase at ambient pressure.[21,22] Yin *et al.* reported three phase transitions starting with the room temperature (RT) to the low temperature (LT) *Pbca* phase at 0.1 GPa, followed by a LT + HP (monoclinic $P2_1/a$) phase at ~1.6 GPa, and finally a completed transition to the monoclinic $P2_1/a$ HP phase ~5.2 GPa and amorphization above ~6 GPa, highlighting the intrinsic flexibility and pressure sensitivity of RP structures (Fig. 4a and b).[21] Similarly, Yuan *et al.* also reported a sequence of phase transitions beginning with an isostructural phase transition observed at around 0.17 GPa evidenced by the appearance of several new peaks in the XRD spectra and the abrupt shift of the first reflection (Fig. 4c) resulting in more staggered octahedra along with rearrangement of the BA organic cations (Fig. 4d).[22] The appearance of further reflections at around 2 GPa (Fig. 4c) indicates a second phase transition likely corresponding to an orthorhombic (*Pbca*) → monoclinic ($P2_1/a$) transition resulting in a disordered structure with uncorrugated inorganic layers (Fig. 4d).[22] These transitions are driven by a combination of increased octahedral tilting, the disruption of long-range order under compression, and the flexibility and bulkiness of the BA spacer cation, which facilitates layer sliding.[22] In contrast, $(PEA)_2PbI_4$ (PEA = phenethylammonium) with a rigid PEA organic spacer has been shown to

This journal is © The Royal Society of Chemistry 2026

Open Access Article. Published on 28 Oktober 2025. Downloaded on 16.02.26 09:35:21.
This article is licensed under a Creative Commons Attribution-NonCommercial 3.0 Unported Licence.

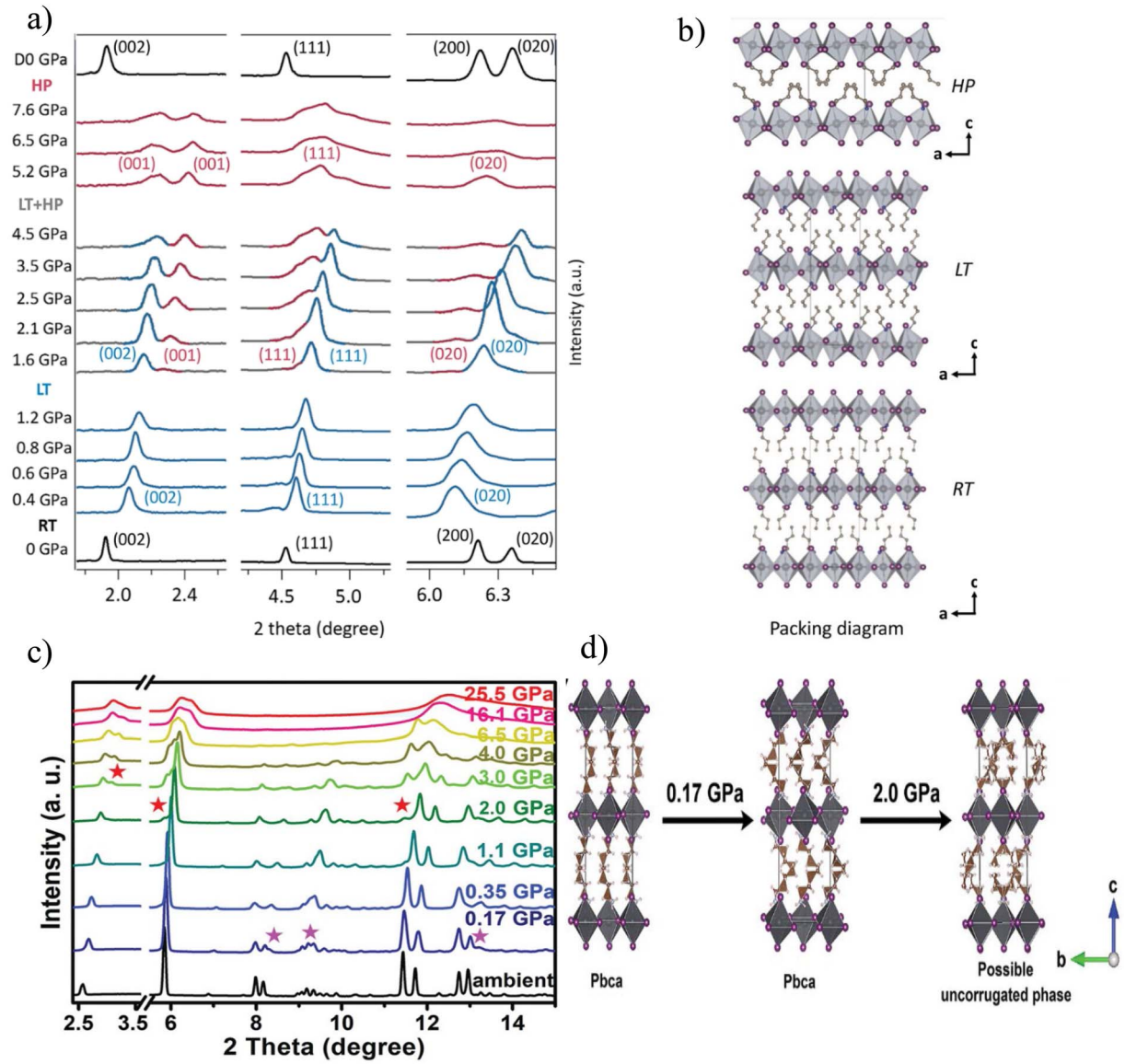

Fig. 4 Sequential phase transitions of RP-type $(BA)_2PbI_4$. (a) *In situ* XRD spectra upon compression to 7.6 GPa and (b) schematic of crystal structures in the RT, LT, and HP phases. Reproduced from ref. 21 with permission from American Chemical Society, copyright 2018. (c) XRD spectra upon compression to 25.5 GPa and (d) schematic of change in the crystal structure from ambient pressure to 2.0 GPa. Reproduced from ref. 22 with permission from Wiley-VCH GmbH, copyright 2019.

undergo a more subtle transition.[19,51] Liu *et al.* reported considerable broadening of the XRD peaks beyond 10.2 GPa, indicating distortion of the crystal lattice under high pressure (Fig. 5a), whilst the equatorial and axial Pb–I bond lengths were found to contract significantly upon compression from 0 to 6 GPa (Fig. 5b) and further confirmed by the theoretical crystal structures at 0 and 4 GPa, respectively, which underlined significant out-of-plane squeezing of the organic part.[19] Thus, these results suggest anisotropic compression and a lack of distortion between 0 and 6 GPa.[19] In another study, Guo *et al.* reported that $(PEA)_2PbI_4$ maintains its layered orthorhombic symmetry until ~5.8 GPa, followed by a subtle order-disorder transition evidenced by the observed broadening in the XRD spectra (Fig. 5c) involving realignment of phenyl rings resulting in a transition from AB (perpendicular) to AA (parallel) arrangement of the PEA spacer cations (Fig. 5d).[51]

3.2. DJ-type 2D perovskites

DJ systems, which incorporate more rigid organic spacers, undergo more subtle phase transitions which are often isostructural in nature such as those observed in $(2meptH_2)PbCl_4$ (2mept = 2-methyl-1,5-diaminopentane) (Fig. 6a)[34] and (API) $PbBr_4$ (API = *N*-(3-aminopropyl)imidazole) (Fig. 6b).[46] In $(2meptH_2)PbCl_4$ only broadening of the ADXRD peaks is observed upon compression (Fig. 6c) along with significant unit cell volume collapse at 2.1 GPa (Fig. 6d), suggesting an isostructural phase transition at 2.1 GPa.[34] Similarly, for (API)$PbBr_4$ again only broadening of the XRD peaks is observed upon

Open Access Article. Published on 28 Oktober 2025. Downloaded on 16.02.26 09:35:21.
This article is licensed under a Creative Commons Attribution-NonCommercial 3.0 Unported Licence.

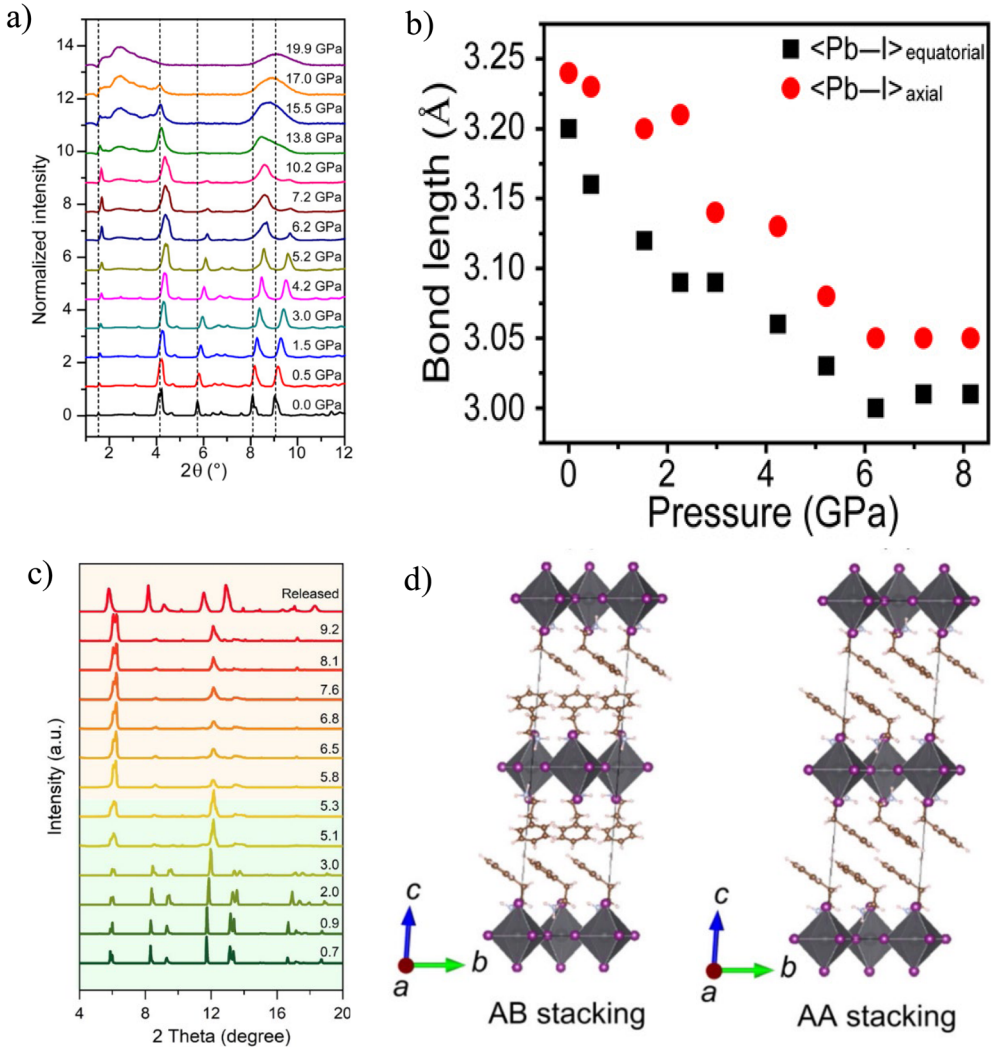

Fig. 5 Subtle structural transition of RP-type $(PEA)_2PbI_4$. (a) XRD spectra upon compression to 19.9 GPa and (b) Pb–I bond lengths as functions of pressure. Reproduced from ref. 19 with permission from American Association for the Advancement of Science, copyright 2019. (c) XRD spectra upon compression to 9.2 GPa and (d) crystal structures showing both AB and AA stacking arrangements. Reproduced from ref. 51 with permission from American Chemical Society, copyright 2019.

compression (Fig. 6e), once again suggesting an isostructural phase transition at around 2.7 GPa evidenced by the appearance of a new peak in the Raman spectra beyond 2.7 GPa (Fig. 6f).[46] Furthermore, an abrupt decrease in both the cell parameters (Fig. 6g) and unit cell volume is observed at around 2.7 GPa (Fig. 6h), providing further evidence of the isostructural phase transition at around 2.7 GPa.[46] DJ systems can also resist pressure-induced reorganization until much higher pressures. When deformation finally occurs, irreversible transitions to disordered or amorphous states can occur, such as those observed in 3AMP-based compounds (3AMP = 3-(aminomethyl) piperidinium).[25] Kong *et al.* observed monotonic shifts of the diffraction peaks to higher 2θ angles followed by structural collapse and irreversible amorphization at higher pressures.[25] It should be noted that the pressure-driven amorphization was a progressive process rather than a sharp transition.[25]

3.3. Effects of spacer geometry and rigidity

Spacer geometry and rigidity can also play a central role in pressure response. Soft spacers such as BA and CMA (cyclohexylmethylammonium) offer greater flexibility and thus allow for more prominent pressure responses leading to sequential phase transitions previously discussed for $(BA)_2PbI_4$[21,22] and significant negative linear compressibility (NLC) in $(CMA)_2PbI_4$ as discussed later.[36] In contrast, systems with rigid π-conjugated spacers such as PEA, have been found to restrict lattice adjustment and can induce octahedral distortions under compression. For instance, octahedral distortion exhibited in RP systems incorporating PEA, *i.e.*, $(PEA)_2PbX_4$ (X = I, Br, Cl), often leads to deformation of the Pb–X framework as observed in $(PEA)_2PbBr_4$ (ref. 27 and 52) and $(PEA)_2PbCl_4$.[30] Similarly, Liu *et al.* observed a greater resistance to compression for $(PEA)_2PbI_4$,[19] while Gao *et al.* observed broad band XRD peaks upon compression attributed to deformation of the PbI_4 skeleton.[51]

 This journal is © The Royal Society of Chemistry 2026

Open Access Article. Published on 28 Oktober 2025. Downloaded on 16.02.26 09:35:21.
This article is licensed under a Creative Commons Attribution-NonCommercial 3.0 Unported Licence.

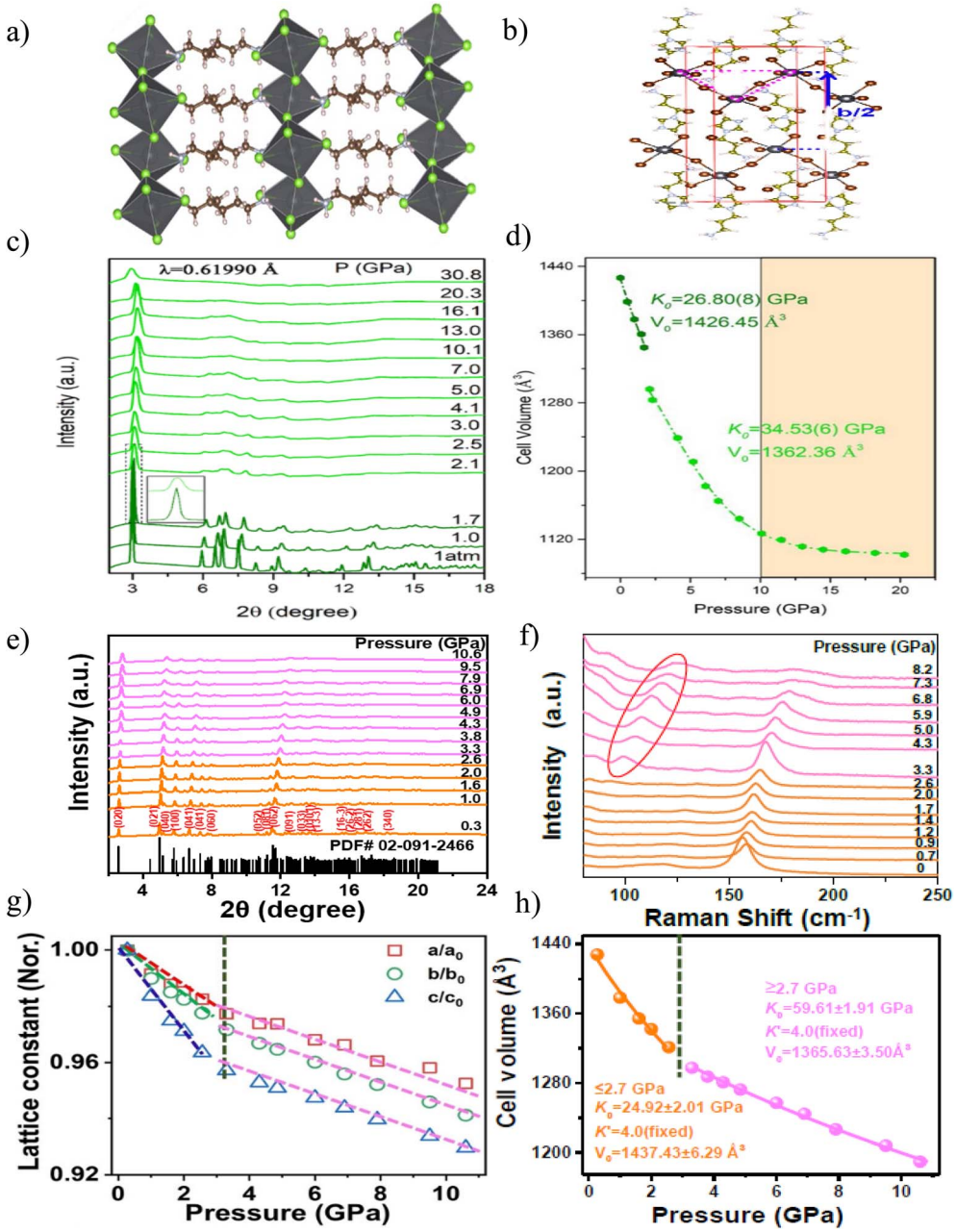

Fig. 6 Pressure-induced structural changes in DJ-type 2D HOIPs with rigid spacers. (a) Crystal structure at ambient pressure of $(2meptH_2)PbCl_4$. Reproduced from ref. 34 with permission from the Royal Society of Chemistry, copyright 2023. (b) Crystal structure at ambient pressure of (API) $PbBr_4$. Reproduced from ref. 46 with permission from Wiley-VCH GmbH, copyright 2024. (c) and (d) *In situ* ADXRD spectra upon compression to 30.8 GPa and unit cell volume as a function of pressure of $(2meptH_2)PbCl_4$. Reproduced from ref. 34 with permission from the Royal Society of Chemistry, copyright 2023. (e)–(h) *In situ* XRD spectra upon compression to 10.6 GPa, Raman spectra upon compression to 8.2 GPa, normalized unit cell parameters as functions of pressure, and unit cell volume as a function of pressure of (API)$PbBr_4$. Reproduced from ref. 46 with permission from Wiley-VCH GmbH, copyright 2024.

However, rigid spacers can also induce more complex phase diagrams. For example, triazolium-based perovskites exhibit four distinct polymorphs under pressure, as observed in Tz_2PbBr_4 (Fig. 7a) which was found to undergo three separate phase transitions evidenced by significant changes in the Raman spectra upon compression (Fig. 7b).[56] First, the splitting of the δC–H, δNCN and γN–H modes at 1251.0, 949.3, and 722.3 cm^{-1} is observed above 2.4 GPa (phase II), which is then followed by further significant changes at 6 GPa where two high-pressure phases (phase II and phase III) coexist, and lastly weak changes of the Raman bands in the lattice mode region are observed up to 8 GPa followed by significant broadening above 8.5 GPa indicating a third phase transition (phase III to phase IV) between 8 and 8.5 GPa.[56]

Frequently, isostructural phase transitions have been observed in 2D HOIPs with both soft and rigid spacers. For

Open Access Article. Published on 28 Oktober 2025. Downloaded on 16.02.26 09:35:21.
This article is licensed under a Creative Commons Attribution-NonCommercial 3.0 Unported Licence.

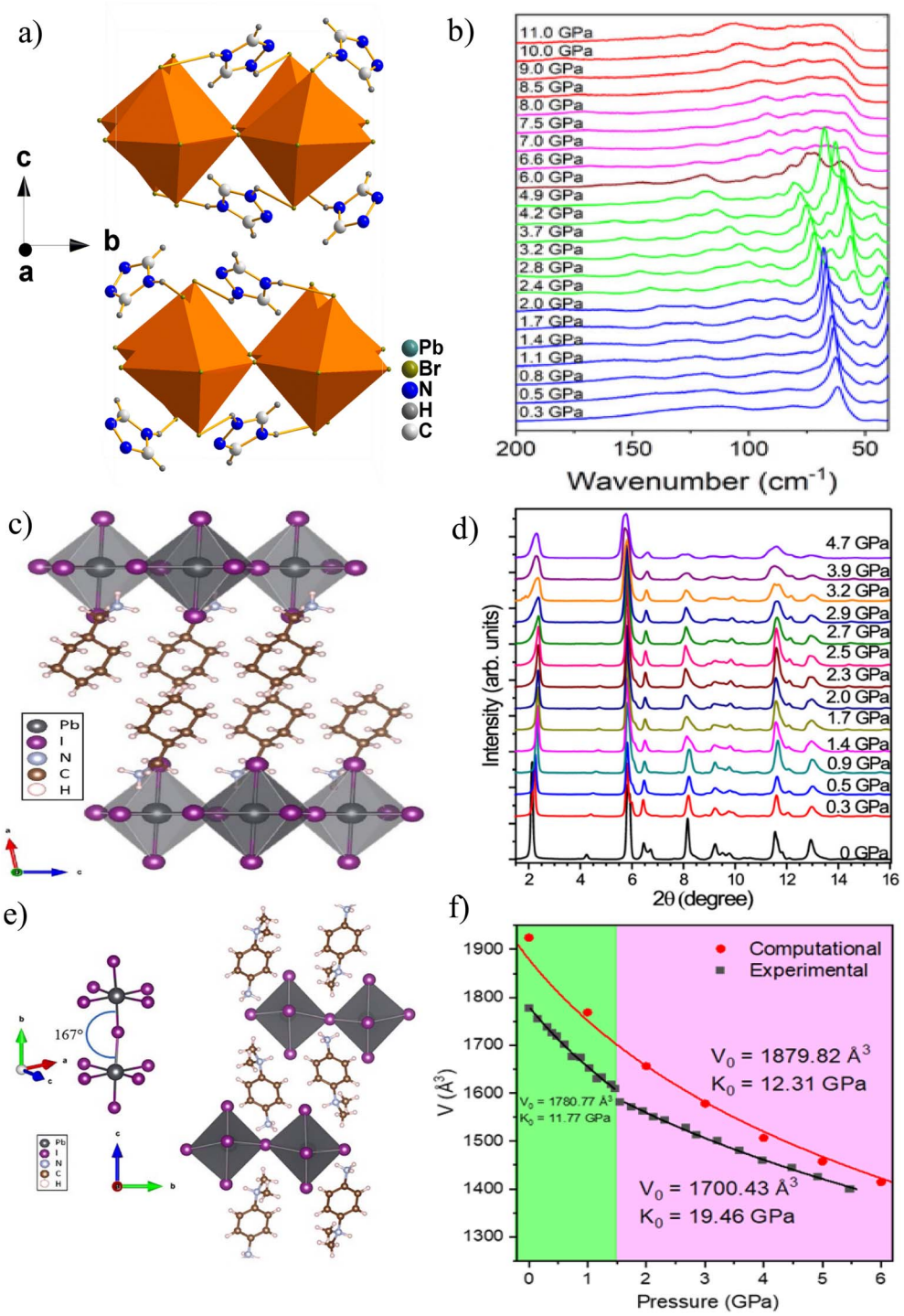

Fig. 7 Space-influenced pressure-induced structural changes of 2D HOIPs. (a) Crystal structure of Tz_2PbBr_4 at ambient pressure and (b) representative Raman spectra of Tz_2PbBr_4 in the 200–40 cm^{-1} range. Reproduced from ref. 56 with permission from the Royal Society of Chemistry, copyright 2024. (c) Crystal structure of $(CMA)_2PbI_4$ at ambient pressure and (d) ADXRD spectra upon compression at selected pressures. Reproduced from ref. 36 with permission from American Chemical Society, copyright 2023. (e) Crystal structure of $DPDAPbI_4$ at ambient pressure and (f) normalized unit cell volume as a function of pressure. Reproduced from ref. 45 with permission from Wiley-VCH GmbH, copyright 2025.

example, an isostructural phase transition was observed in soft RP-type $(CMA)_2PbI_4$ (CMA = cyclohexylmethylammonium) (Fig. 7c) evidenced by the lack of significant changes in the XRD spectra (Fig. 7d).[36] Similarly, an isostructural phase transition was also observed in rigid DJ-type $DPDAPbI_4$ (DPDA = *N*,*N*-dimethylphenylene-*p*-diammonium) (Fig. 7e), again evidenced by a lack of significant changes in the XRD spectra and further

This journal is © The Royal Society of Chemistry 2026

Open Access Article. Published on 28 Oktober 2025. Downloaded on 16.02.26 09:35:21.
This article is licensed under a Creative Commons Attribution-NonCommercial 3.0 Unported Licence.

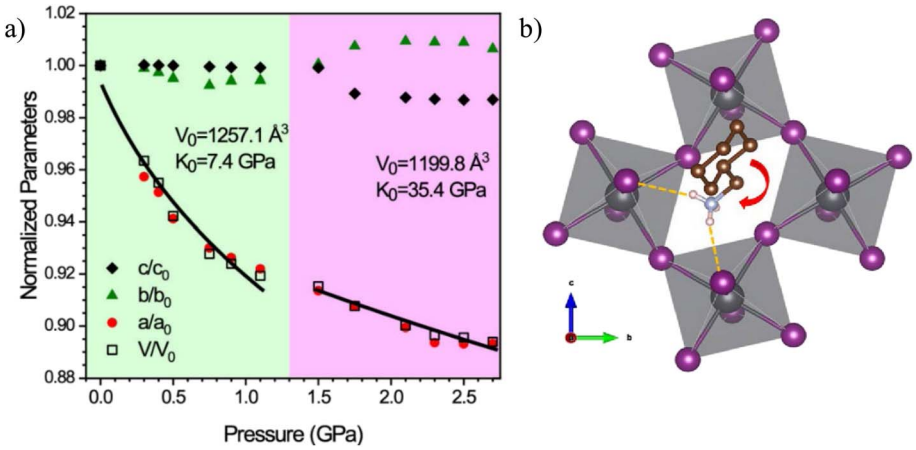

Fig. 8 Pressure-induced rare phenomena in $(CMA)_2PbI_4$. (a) Normalized unit cell parameters and unit cell volume as functions of pressure showing NLC along the *b* direction and (b) possible rotation of the CMA ring (shown by a red arrow) along the *a*-axis. Reproduced from ref. 36 with permission from American Chemical Society, copyright 2023.

confirmed by a discontinuity in the experimental Rietveld refined unit cell volume at around 1.5 GPa (Fig. 7f).[45]

For both RP and DJ systems, when compression pressure is sufficiently high, pressure-induced amorphization is often observed but with different transition pressures. In general, RP systems with soft spacers exhibit a higher threshold for amorphization, typically in the range of 5–10 GPa, whereas DJ systems have a relatively lower amorphization threshold (2–3 GPa), often preceded by an order-disorder transition. The different amorphization thresholds between the two systems are associated with the spacer rigidity and its interplay with the inorganic octahedra, such that external stress is mitigated by the spacer component of RP systems whereas the inorganic moiety of the DJ systems acts as the primary responder to compression. Nonetheless, the amorphization threshold compared to that for pure inorganic perovskites such as $CsPbBr_3$ (typically > 20 GPa) is much lower due to the lack of an organic spacer as a disorder precursor and contributor. Correspondingly, the reversibility of the amorphization–recrystallization cycles can be rationalized by examining several factors including spacer rigidity and flexibility, layer thickness, hydrogen bonding character, and experimental conditions. Typically, both RP and DJ-type 2D HOIPs were found to exhibit either full or partial reversibility upon decompression, whereas irreversible amorphization or disordering is observed in inorganic perovskites such as $CsPbBr_3$. These findings highlight how spacer rigidity and conformational freedom modulate both the mechanical anisotropy and phase stability of 2D HOIPs, offering a pathway to tailor their pressure resilience through molecular design.

3.4. Pressure-induced rare phenomena

Furthermore, the type of organic spacer (either soft or rigid) can also result in the rare or uncommon pressure-induced

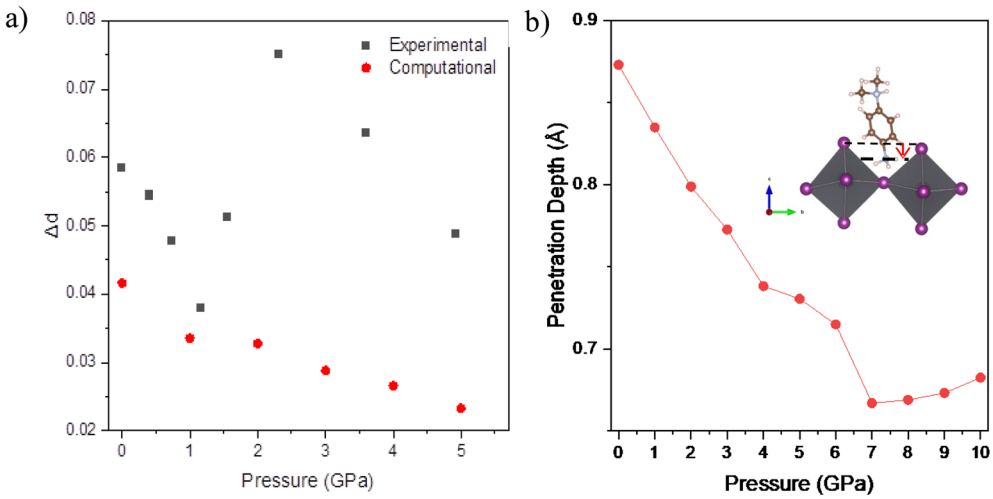

Fig. 9 Pressure-induced uncommon phenomena in $DPDAPbI_4$. (a) Bond length distortion as a function of pressure showing relaxation of octahedral distortion at low pressure and (b) penetration depth of the DPDA spacer as a function of pressure. Reproduced from ref. 45 with permission from Wiley-VCH GmbH, copyright 2025.

Open Access Article. Published on 28 Oktober 2025. Downloaded on 16.02.26 09:35:21. This article is licensed under a Creative Commons Attribution-NonCommercial 3.0 Unported Licence.

Table 1 Pressure-induced phase transitions or structural modifications in 2D hybrid perovskites

Perovskite	Type	Spacer type	Phase transitions/structural modifications	Critical pressure (GPa)	Ref.
$(PEA)_2PbI_4$	RP	Rigid	AB → AA stacking	5.8	51
$(BA)_2PbI_4$	RP	Soft	Isostructural (*Pbca* I → *Pbca* II) → amorphous	∼0.5 and ∼4.77	20
			Pbca (1*b* → 1*a*) → $P2_1/a$ → amorphous	0.1, ∼1.6, and ∼5.2	21
			Pbca → *Pbca* → uncorrugated phase → $P2_1/a$	0.17 and 2, 3	22
$(BA)_2PbBr_4$	RP	Soft	I ($PbBr_6$ octahedra and BA tilting)	∼3.7	26
			Pbca → $P2_1/c$	0.3	28
$(BA)_2(MA)Pb_2Br_7$	RP	Soft	I ($PbBr_6$ octahedra tilting and BA and MA rotation)	3.4–4.8	26
			II ($PbBr_6$ octahedra tilting and BA and MA rotation)	4.8–8.1	
$(OA)_2PbI_4$	RP	Soft	LP (*Pbca*) → (LP + HP (*Pbca* + $P2_1/a$) → HP ($P2_1/a$) → amorphous	∼0.5, ∼2.17, and ∼7.29	20
$(DDA)_2PbI_4$	RP	Soft	LP (*Pbca*) → LP + HP (*Pbca* + $P2_1/a$) → HP ($P2_1/a$) → amorphous	∼0.8, ∼4.09, and ∼10.17	20
$(PMA)_2PbI_4$	RP	Rigid	*Pbca* → *Pccn* → isostructural	4.6 and 7.7	29
$(GA)_2PbI_4$	RP	Soft	Isostructural	5.5	32
$(BzA)_2PbBr_4$	RP	Rigid	Isostructural	0.15–0.25	33
$(CMA)_2PbI_4$	RP	Soft	Isostructural phase transition and NLC → amorphous	∼1.1–1.3	36
MHy_2PbI_4	RP	Soft	Phase II (*Pmcn*) → phase V (*Pmmn*) → phase VI ($Pmn2_1$) → phase VII ($P2_1$)	0.22, 1.15, and 3.00	41
MHy_2PbBr_4	RP	Soft	Phase III ($Pmn2_1$) → phase IV ($P2_1$) → phase V ($P2_12_12_1$)	∼4 and ∼4.4	43
			Phase III ($Pmn2_1$) → phase IV ($P2_1$)	∼4	55
$(Tz)_2PbBr_4$	RP	Rigid	Phase I → phase II → phase III → phase IV	2.4, 6, and 8–8.5	56
$(2meptH_2)PbCl_4$	DJ	Rigid	Isostructural (unit cell volume collapse)	2.1	34
$IMMHyPbBr_4$	DJ	Rigid	First order (abrupt shifts of Raman modes)	∼1.25–1.53	40
$(API)PbBr_4$	DJ	Rigid	Isostructural (abrupt unit cell volume change)	2.7	46
$DPDAPbI_4$	DJ	Rigid	Isostructural (unusual octahedral distortion) → amorphous	∼0–2	45

phenomena in 2D HOIPs. For example, RP-type $(CMA)_2PbI_4$ exhibits a prominent negative linear compressibility (NLC) which is observed between 1.1 and 1.2 GPa evidenced by the increase in the *b* parameter (Fig. 8a), which is in stark contrast to both $(PEA)_2PbI_4$ and $(BA)_2PbI_4$.[36] The observed NLC is believed to result from possible rotation of the CMA ring along the *a*-axis thus enhancing the stacking efficiency but subsequently causing a slight expansion of the *b*-axis (Fig. 8b).[36] Such NLC behavior resulting in enhanced anisotropic pressure-tuned stacking efficiency involving a soft and highly flexible spacer cation was not previously observed in other 2D HOIPs.[36] In contrast, the rigidity of the DPDA spacer in DJ-type $DPDAPbI_4$ plays a significant role in the pressure behavior; in particular distortion analysis underlined the uncommon phenomenon of reduced octahedral distortion until 1 GPa followed by an abrupt enhancement between 1 and 2 GPa (Fig. 9a) with the initial decrease believed to be caused by the deep insertion of the DPDA spacer cation into the PbI_6 octahedral pockets resulting in decreased penetration depth upon compression (Fig. 9b).[45]

Overall, pressure is a highly effective method for modifying the structures of 2D HOIPs in particular by inducing phase transitions, octahedral tilting and distortion, and amorphization. The geometry and rigidity of the organic spacer cations can not only influence the pressure response but can also at times result in rare phenomena. Table 1 summarizes key structural transitions reported in representative 2D HOIPs under compression.

This table summarizes key high-pressure structural responses of 2D perovskites, classified by phase type (RP or DJ), spacer rigidity, and inorganic composition. Phase transitions typically occur at relatively low pressures (<5 GPa), reflecting the structural softness of 2D HOIPs compared to their 3D counterparts. RP systems with soft organic spacers (*e.g.*, BA and CMA) undergo sequential phase transitions and amorphization, while those with rigid aromatic spacers (*e.g.*, PEA) exhibit subtle or order–disorder transitions. DJ systems, stabilized using bifunctional spacers, generally show higher resistance to compression, often undergoing isostructural transitions or gradual amorphization at elevated pressures. The table highlights the influence of spacer geometry and connectivity on compressibility and phase stability.

4. Tuning optoelectronic properties with pressure

Whilst high pressure has been shown to be highly effective at inducing structural modifications through phase transitions primarily caused by changes in the octahedral distortion and interlayer interactions, high pressure has also been shown to effectively tune the optoelectronic properties (*i.e.* PL emissions and bandgaps) of 2D HOIPs thus making high pressure a promising method for tuning such properties to make them ideal candidates for several applications, in particular solar cells and light emitting diodes. In this section the pressure-induced optoelectronic properties of 2D HOIPs are discussed showing how pressure can cause changes to the bandgaps, PL emissions, and charge carrier lifetimes, whilst also enabling metastable states with enhanced properties in certain compounds.

 This journal is © The Royal Society of Chemistry 2026

Open Access Article. Published on 28 Oktober 2025. Downloaded on 16.02.26 09:35:21.
This article is licensed under a Creative Commons Attribution-NonCommercial 3.0 Unported Licence.

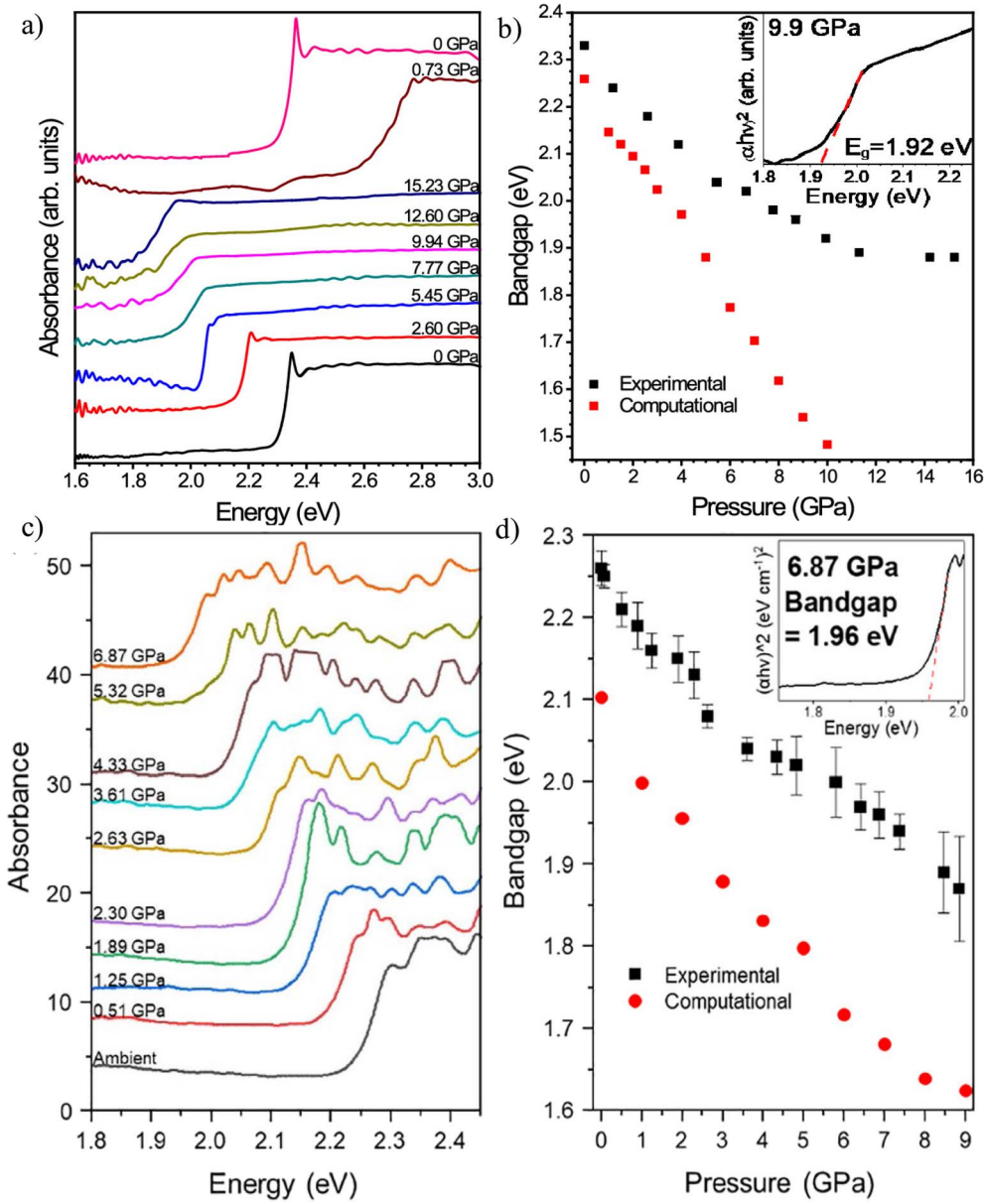

Fig. 10 Pressure-induced optical absorbance behavior of 2D HOIPs with differing organic spacers. (a) *In situ* UV-vis absorption spectra upon compression to 15.23 GPa and (b) bandgap as a function of pressure for $(CMA)_2PbI_4$. Reproduced from ref. 36 with permission from American Chemical Society, copyright 2023. (c) *In situ* UV-vis absorption spectra upon compression to 6.87 GPa and (d) bandgap as a function of pressure for $DPDAPbI_4$. Reproduced from ref. 45 with permission from Wiley-VCH GmbH, copyright 2025.

4.1. General trend of bandgap evolution

One of the most prominent pressure responses in 2D HOIPs is the modulation of the bandgap. Several bandgap trends can occur upon compression with the most common one being a gradual redshift of the absorption edge (gradual bandgap narrowing) upon compression which was observed in several previously studied 2D HOIPs. Ratté *et al.* observed a continuous gradual redshift of the absorption edge until 15.23 GPa (Fig. 10a) corresponding to a significant bandgap reduction from 2.33 to 1.89 eV (ΔE_g = 0.44 eV) upon compression to 11.3 GPa (Fig. 10b) for soft RP-type $(CMA)_2PbI_4$, in good agreement with the DFT calculated bandgap values, and the bandgap was found to remain direct throughout the compression process.[36] The authors attributed the monotonic bandgap narrowing and constant direct nature to anisotropic contraction of the PbI_6 octahedra as opposed to tilting evidenced by the compression of the axial and equatorial Pb–I bond lengths with the latter showing greater compression at high pressure.[36] Similarly, Kutty *et al.* also observed a gradual continuous redshift of the absorption edge upon compression beyond 6.87 GPa (Fig. 10c) corresponding to a significant monotonic bandgap reduction from 2.26 to 1.87 eV (ΔE_g = 0.39 eV) upon compression to 8.84 GPa (Fig. 10d) for rigid DJ-type $DPDAPbI_4$, again in excellent agreement with the DFT computations and

Open Access Article. Published on 28 Oktober 2025. Downloaded on 16.02.26 09:35:21.
This article is licensed under a Creative Commons Attribution-NonCommercial 3.0 Unported Licence.

once again the direct bandgap nature was maintained throughout compression.[45] However, unlike for $(CMA)_2PbI_4$, the monotonic bandgap reduction for $DPDAPbI_4$ was found to result from the strong correlation between the enhancement of both the N–H···I hydrogen bonding interactions and PbI_6 octahedral distortion at low pressure (>2 GPa) whilst at higher pressure the rigidity of the DPDA spacer and overall electronic configurations collectively determined the optoelectronic properties.[45]

Similar strong correlations between the hydrogen bonding interactions and bandgap evolution were observed in a rigid RP-type system, $(PMA)_2PbI_4$, where (PMA = phenylmethylammonium), with the enhancement of the hydrogen bonding interactions inducing distortion of the PbI_6 octahedra and in turn a significant bandgap narrowing from 2.19 to 1.26 eV (ΔE_g = 0.93 eV).[29] Interestingly, Gao *et al.* observed bandgap narrowing from 2.26 to 1.83 eV (ΔE_g = 0.43 eV) upon compression to 5.8 GPa in another rigid RP-type system, $(PEA)_2PbI_4$, followed by an abrupt jump to 1.95 eV and a direct-to-indirect bandgap transition attributed to the AB to AA stacking arrangement phase transition discussed previously.[51] These results not only underline how the type of organic spacer can influence the bandgap behavior at high pressure but as observed in $(PEA)_2PbI_4$ pressure can also result in deviations away from the general bandgap trends as discussed later.

Overall, all 2D HOIPs, including both RP and DJ types, display universal pressure-induced bandgap narrowing albeit to different extents. Remarkably, compared to classical inorganic 2D materials such as MoS_2, the absolute value of pressure-induced bandgap reduction in 2D HOIPs is exceptionally high, given that most inorganic 2D materials already have low initial bandgaps (*e.g.*, <1.5 eV) and often undergo a transition to a metallic state at moderate pressures. As summarized in Table 3 below, while the general tunability for 2D HOIPs is $\Delta E_g \approx$ 0.5 eV over a 10 GPa range on average, select systems exhibit much greater bandgap reductions – *e.g.*, 1.33 eV and 0.93 eV observed for RP-type $(BA)_2PbI_4$ and $(PMA)_2PbI_4$, respectively.[22,29] Moreover, compared to the DJ type, RP type HOIPs generally show more prominent bandgap reduction, especially with soft spacers due to the larger compressible-pressure range, although some RP systems with rigid spacers may display non-monotonic trends as illustrated below.

4.2. Beyond the norm: blueshifts and non-monotonic trends

One such unusual and intriguing pressure-induced bandgap trend is an initial blueshift of the absorption edge (bandgap widening) at low pressure due to lattice contraction and increased octahedral tilting, which reduces electronic coupling and narrows bandwidths, whilst at higher pressure the bond lengths shorten and Pb–X–Pb bond angles approach linearity, enhancing orbital overlap and resulting in a redshift of the absorption edge (bandgap narrowing). Such a trend was observed previously in $(BA)_2PbI_4$.[21,22] Yin *et al.* observed piezochromic transitions upon compression to 10 GPa (Fig. 11a) evidenced by an initial blueshift of the absorbance peak upon compression to 0.4 GPa followed by a continuous redshift upon further compression and the emergence of a second peak beyond 1.9 GPa whilst broadening beyond 5 GPa indicating the onset of amorphization (Fig. 11b).[21] Theoretical studies indicated a decrease in the Pb–I–Pb bond angle from 150.2° to 144.9° along with an increase in the average equatorial Pb–I bond length from 3.09 Å to ~3.14 Å at 0.4 GPa, thus leading to diminished Pb–I orbital overlap and the subsequent initial blueshift of the absorbance peak.[21] Further compression resulted in the expected opposite trend, the bond angle and average equatorial bond length increased and decreased back to 150.5 Å and 3.09 Å, respectively leading to the continuous redshift of the main absorbance peak and the second peak beyond 1.9 GPa (Fig. 11b).[21] Similarly, Yuan *et al.* also observed an initial abrupt blueshift of the absorption edge (Fig. 11c) and subsequent bandgap widening from 2.28 to 2.37 eV (Fig. 10d) upon compression to 0.22 GPa followed by a continuous redshift (Fig. 11c) and bandgap narrowing to 0.95 eV at around 35 GPa (Fig. 11d).[22] Yuan *et al.* also observed new absorption edges upon compression to 2.2 and 13.1 GPa (Fig. 11c) which they attributed to second and third phase transitions with increased PbI_6 octahedral tilting leading to initial bandgap widening and subsequent decreased tilting and Pb–I bond length shortening resulting in gradual bandgap narrowing (Fig. 11d).[22]

Another unusual pressure-induced bandgap trend that has been observed is that of a continuous redshift of the absorption edge (bandgap narrowing) followed by an abrupt blueshift (bandgap widening) and finally a re-redshift (re-reduction). Such pressure-induced bandgap behavior was previously exhibited in $(PEA)_2PbBr_4$.[27,52] Ren *et al.* observed a prominent redshift of the absorption edge upon initial compression to 10 GPa (significant bandgap narrowing from 2.99 to ~2.5 eV) followed by an abrupt blueshift (bandgap widening) between 10–28.4 GPa and a subsequent re-redshift (re-reduction) between 28.4–48.2 GPa (Fig. 12a and b).[27] Once again the first redshift was attributed to lattice contraction of the crystallized sample while abrupt blueshift was attributed to amorphization causing the distorted $PbBr_6$ octahedra with subsequent contraction of the disordered lattice resulting in re-redshift.[27] Zhang *et al.* also observed a significant redshift of the absorption edge upon compression to ~12 GPa followed by an abrupt blueshift until ~15 GPa and finally a gradual re-redshift until 28.4 GPa (Fig. 12c) resulting in a significant bandgap narrowing from 2.96 to 2.46 eV followed by a slight bandgap widening and gradual re-reduction (Fig. 12d).[52] The initial redshift and significant bandgap reduction were attributed to the soft oriented organic cation layer causing enhanced orbital overlap of Pb s and Br p states.[52] The abrupt blueshift and subsequent bandgap widening were attributed to $PbBr_6$ octahedral distortion leading to reduced compressibility and in turn decreased metal-halide orbital coupling.[52] Finally, the re-redshift and re-reduction of the bandgap were believed to result from the competition of the compression effect with the interlayer bond contraction and lattice distortion.[52]

These diverse pressure-induced bandgap behaviors—monotonic, non-monotonic, or flattened—can be consistently rationalized using the competing effects of bond contraction and octahedral tilting. In soft-spacer (*e.g.* long alkylammonium

 This journal is © The Royal Society of Chemistry 2026

Open Access Article. Published on 28 Oktober 2025. Downloaded on 16.02.26 09:35:21.
This article is licensed under a Creative Commons Attribution-NonCommercial 3.0 Unported Licence.

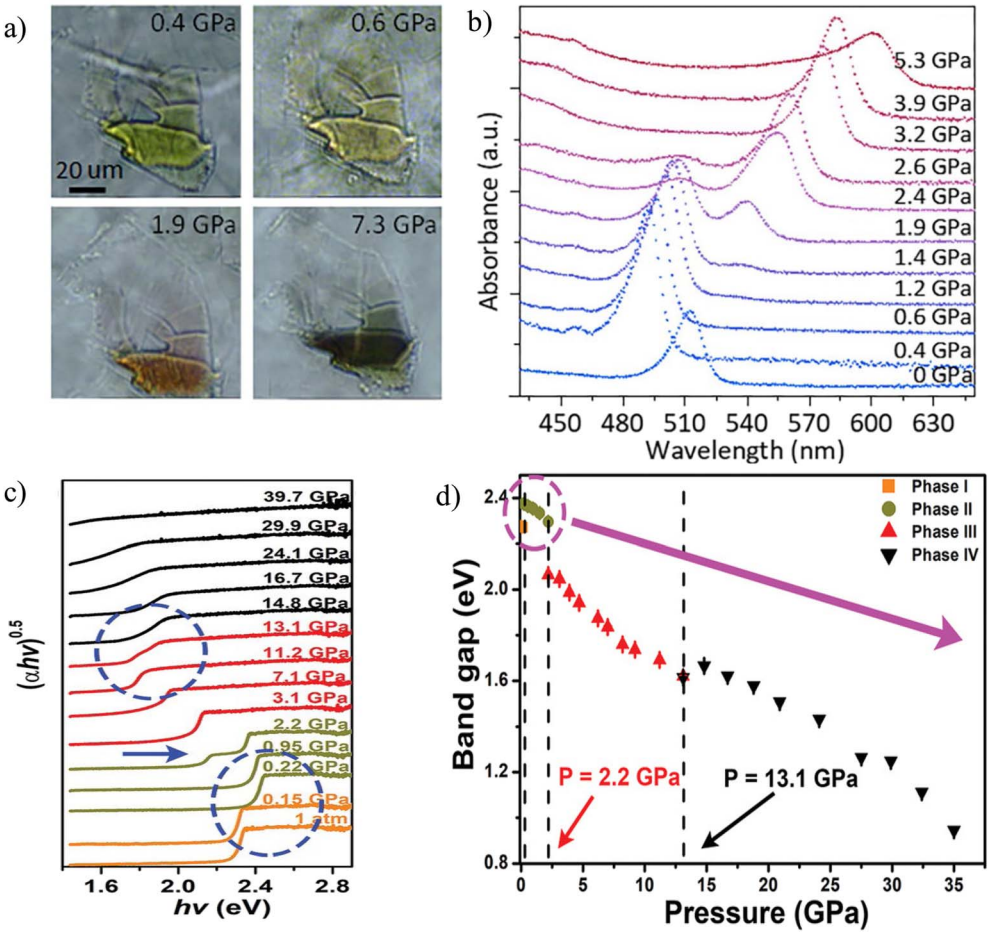

Fig. 11 Pressure-induced optical absorbance behavior of $(BA)_2PbI_4$. (a) Optical images at selected pressures illustrating piezochromism and (b) *In situ* UV-vis absorption spectra. Reproduced from ref. 21 with permission from American Chemical Society, copyright 2018. (c) *In situ* UV-vis absorption spectra upon compression to 39.7 GPa and (d) bandgap as a function of pressure. Reproduced from ref. 22 with permission from Wiley-VCH GmbH, copyright 2019.

chains) RP systems, flexible organic layers accommodate pressure through lattice compression, allowing bond shortening to dominate and yielding continuous bandgap narrowing. In contrast, rigid DJ systems, where the organic layer is more rigid or tightly bound (*e.g.* diammonium linkers or aromatic cations that lock adjacent layers together), often resist direct compression, leading to enhanced octahedral tilting or distortion at lower pressures, which can counteract or even reverse the redshift, leading to bandgap widening. This framework also explains the non-monotonic trends observed in certain systems: an initial redshift arises from bond contraction, followed by a blueshift or bandgap plateau as tilting becomes more pronounced beyond a structural crossover pressure. Recognizing this mechanistic balance provides a unified lens through which it is possible to interpret the system-dependent optical responses seen across 2D HOIP families under compression.

4.3. Photoluminescence: enhancement and quenching pathways

Along with modulation of the bandgap, pressure can also, at times, increase photoluminescence (PL) intensity in many 2D perovskites. This PL enhancement is often attributed to the suppression of non-radiative recombination pathways, such as trap-assisted processes, as pressure passivates defects and reduces lattice strain. Such suppression of trapped states was previously observed in GA-based (GA = guanidinium) 2D HOIPs.[50,53] For example, Chen *et al.* observed a 5-fold PL enhancement upon compression to 1.3 GPa (Fig. 13a) followed by a gradual decrease until quenching at 7 GPa in $(GA)(MA)_2Pb_2I_7$ (Fig. 13b).[50] Interestingly, the PL peak was found to redshift initially followed by an abrupt blueshift until quenching (Fig. 13a and b).[50] The PL enhancement was believed to result from confinement of the charge carriers due to volume contraction upon compression thus leading to increased exciton binding energy, while the gradual decrease in intensity was believed to result from the suppression effect in the emission process.[50] Similarly, Guo *et al.* observed a sharp 12-fold PL enhancement upon compression to 1.59 GPa followed by a gradual decrease until eventual quenching at 9.48 GPa in $(HA)_2(GA)Pb_2I_7$ (Fig. 13c).[53] Upon fitting the PL spectra, the authors observed a strong contribution to the PL emission from trapped states at ambient pressure which then gradually decreases upon compression until 1.59 GPa where the

Open Access Article. Published on 28 Oktober 2025. Downloaded on 16.02.26 09:35:21.
This article is licensed under a Creative Commons Attribution-NonCommercial 3.0 Unported Licence.

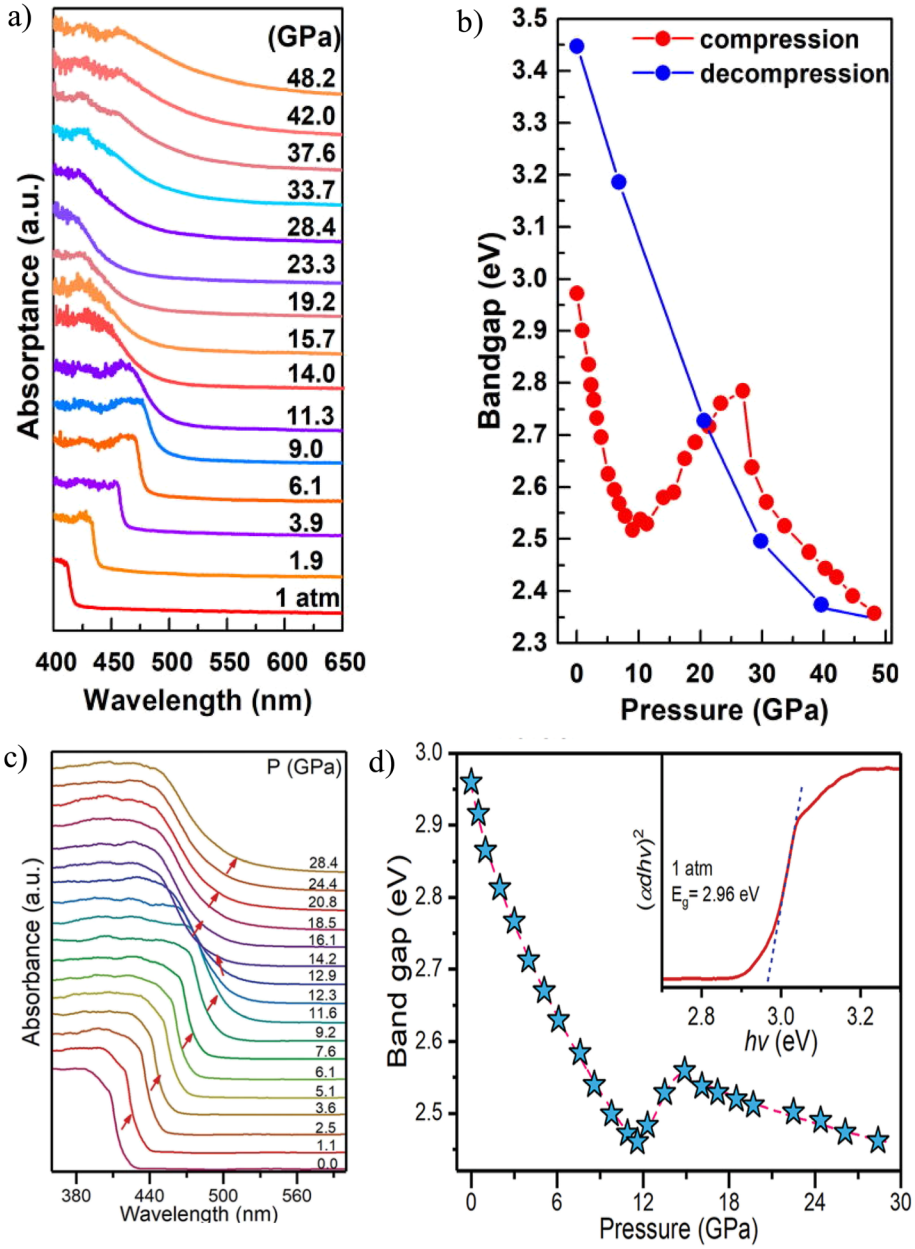

Fig. 12 Pressure-induced optical absorbance behavior of $(PEA)_2PbBr_4$. (a) *In situ* UV-vis absorption spectra upon compression to 48.2 GPa and (b) bandgap as a function of pressure. Reproduced from ref. 27 with permission from AIP Publishing, copyright 2020. (c) *In situ* UV-vis absorption spectra upon compression to 28.4 GPa and (d) bandgap as a function of pressure. Reproduced from ref. 52 with permission from Wiley-VCH GmbH, copyright 2018.

contribution is fully from free excitons (FEs) (Fig. 13d).[53] More significantly, Guo *et al.* reported an extraordinary 72-fold PL enhancement for RP-type $(BA)_2(GA)Pb_2I_7$ upon compression to 2.1 GPa, which was attributed to the suppression of exciton trapping.[39] Thus, it is believed that PL enhancement in general is associated with the suppression of carrier trapping due to reduced distortion of the Pb–I sublattice leading to a decrease in the energy barrier between the FE and trapped states.[53]

In comparison to the RP-type and ACI-type systems, DJ-type 2D HOIPs tend to exhibit less prominent PL enhancements upon compression. For example, the PL intensity for $DPDAPbI_4$ exhibits a slightly more than twofold enhancement upon compression to 1.5 GPa followed by a gradual decrease until eventual quenching at 5.6 GPa.[45] For $(API)PbBr_4$, the FE PL peak shows an approximately fivefold enhancement upon compression to 2.7 GPa followed by a gradual decrease until quenching at around 6 GPa.[46] Furthermore, all the observed PL enhancements were in excellent agreement with the corresponding isostructural phase transitions.[45,46] Overall, it appears that all RP-, DJ- and ACI-type 2D HOIPs undergo initial pressure-induced PL enhancements followed by quenching, although the associated PL mechanisms may differ, as discussed below.

This journal is © The Royal Society of Chemistry 2026

Open Access Article. Published on 28 Oktober 2025. Downloaded on 16.02.26 09:35:21.
This article is licensed under a Creative Commons Attribution-NonCommercial 3.0 Unported Licence.

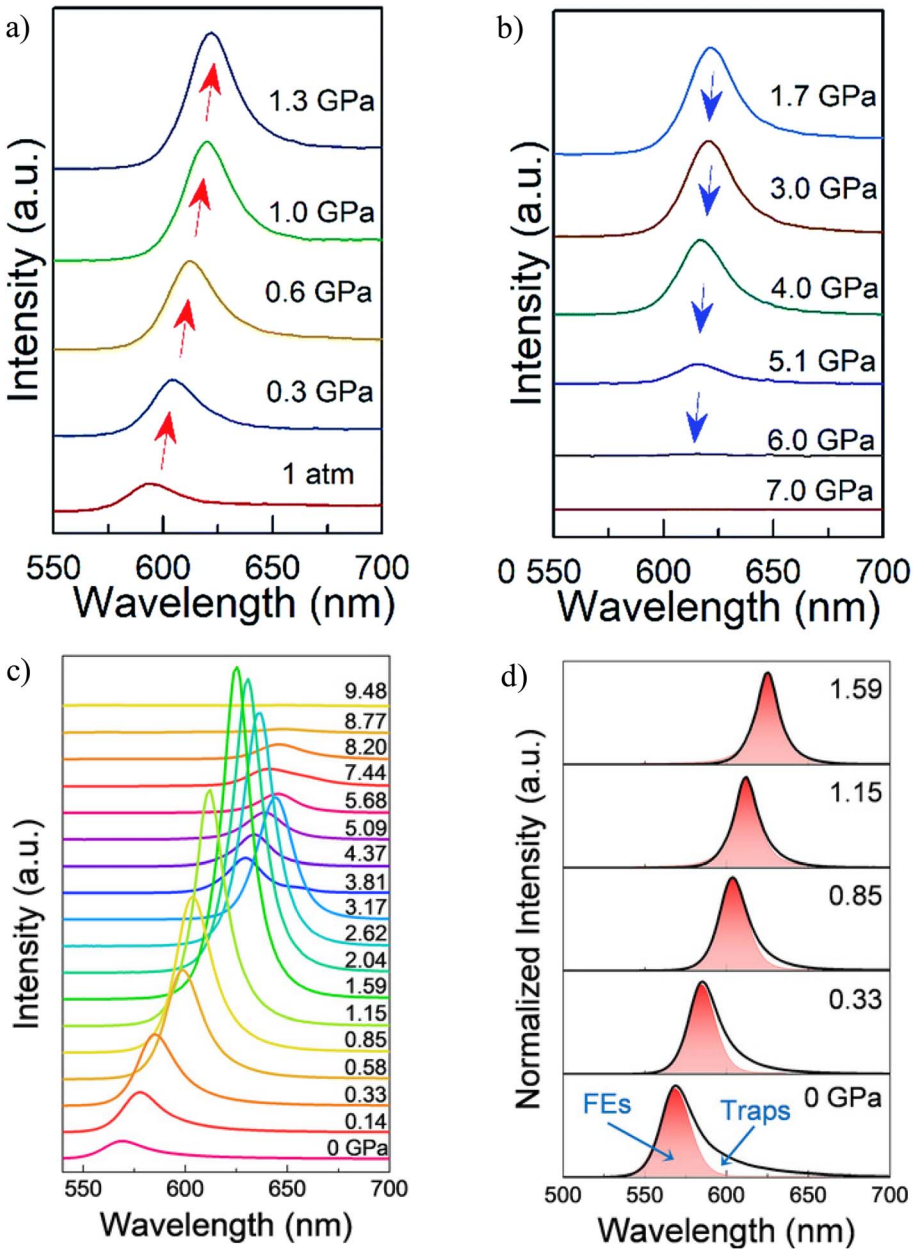

Fig. 13 Pressure-induced PL enhancement of GA-based 2D HOIPs. (a) and (b) *In situ* PL spectra upon compression to 1.3 and 7.0 GPa respectively for $(GA)(MA)_2Pb_2I_7$. Reproduced from ref. 50 with permission from the Royal Society of Chemistry, copyright 2019. (c) and (d) *In situ* PL spectra upon compression to 9.48 GPa and fitted PL spectra at selected pressures for $(HA)_2(GA)Pb_2I_7$. Reproduced from ref. 53 with permission from Wiley-VCH GmbH, copyright 2020.

4.4. From free excitons to STEs: pressure-driven PL mechanisms

Notably, pressure not only tunes PL intensity but can also qualitatively change its nature. In several lead-based RP perovskites, initial PL emission is associated with free excitons followed by broadband emission emerging under moderate pressure (~4–6 GPa), associated with self-trapped excitons (STEs). Such behavior was previously exhibited in RP-type $(PEA)_2PbBr_4$, where Zhang *et al.* also observed a gradual redshift and intensity decrease of the initial FE PL peak and the emergence of the broadband STE peak at around 4 GPa in RP-type $(PEA)_2PbBr_4$ (Fig. 14a).[52] The presence of the STE peak was attributed to increased lattice distortion upon compression due to localization of charge carriers leading to stable STEs, while the lack of lattice distortion at low pressure means stable STEs cannot form, and thus only the FE peak is visible (Fig. 14a).[52] Similarly, Mączka *et al.* observed an initial linear redshift of the FE PL peak upon compression to ~2 GPa followed by a less pronounced redshift between 2 and 6 GPa and the emergence of a broadband STE PL peak at 4.42 GPa in RP-type Tz_2PbBr_4 (Fig. 14b).[56] The redshift until ~2 GPa was attributed to substantial shortening of the Pb–Br bonds while the less pronounced shift between 2 and 6 GPa was attributed to tilting

Open Access Article. Published on 28 Oktober 2025. Downloaded on 16.02.26 09:35:21.
This article is licensed under a Creative Commons Attribution-NonCommercial 3.0 Unported Licence.

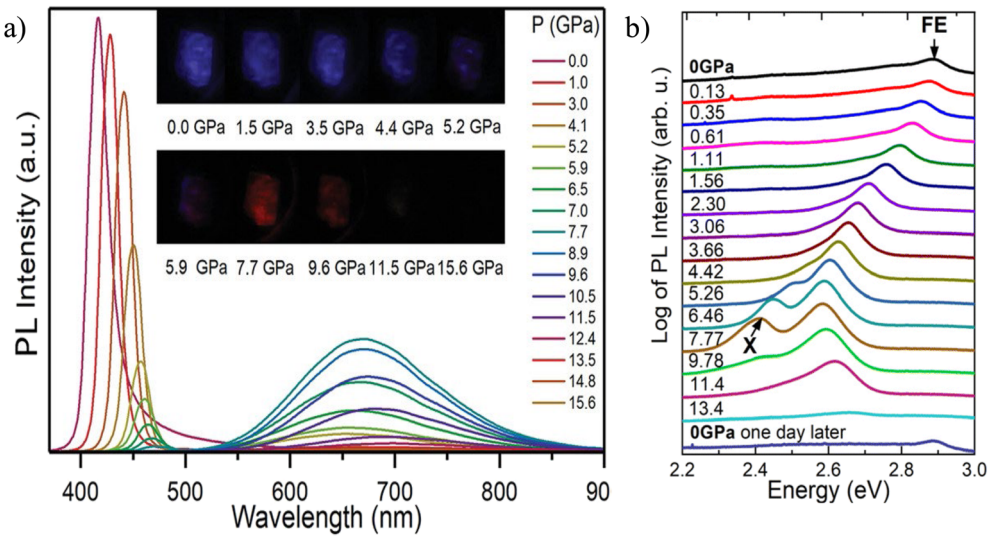

Fig. 14 Pressure-induced change in the PL nature of RP-type 2D HOIPs. (a) *In situ* PL spectra upon compression to 15.6 GPa of $(PEA)_2PbBr_4$. Reproduced from ref. 52 with permission from Wiley-VCH GmbH, copyright 2018. (b) *In situ* PL spectra upon compression to 13.4 GPa of Tz_2PbBr_4. Reproduced from ref. 56 with permission from the Royal Society of Chemistry, copyright 2024.

and distortion of the $PbBr_6$ octahedra, consistent with the first pressure-induced phase transition at around 2 GPa.[56] The lack of significant shift of the FE peak between 6–8 GPa but the continued intensity increase was attributed to the compensation of the Pb–Br bond length shortening by the octahedral tilting and distortion, consistent with the second pressure-induced phase transition at around 6 GPa, and finally an abrupt blueshift and decreased intensity beyond 8 GPa of both the FE and STE peaks is observed attributed to stronger pressure-induced octahedral tilting and distortion in comparison to Pb–Br bond length shortening, consistent with the third and final pressure-induced phase transition between 8 and 8.5 GPa.[56]

Building on this mechanistic picture, Guo *et al.* presented a concise structure-PL map that links how the inorganic sheets and organic spacers accommodate compression to the balance between free-exciton and self-trapped emission for RP-type HOIPs.[39] They showed that pressure which primarily reduces intralayer disorder while tightening interlayer coupling tends to suppress trap-assisted or STE-like features and steer the spectra toward brighter, more symmetric FE emission; conversely, when compression is absorbed mainly through enhanced octahedral tilting or layer misregistry, STE signatures are stabilized and can overtake FE. Viewed this way, the appearance, crossover, or quenching of broad STE bands across RP families—and the possibility of reproducing FE-dominated emission by chemically emulating the pressure-optimized packing through spacer choice—follow from the same structural lever, offering a transferable design rule for tuning emissive pathways under pressure.

DJ-type 2D HOIPs also exhibit both FE and STE contributions, but their pressure evolution often contrasts with RP analogues. In (API)$PbBr_4$, an initially STE-dominated spectrum narrows into an FE-like line under modest compression as enhanced carrier delocalization suppresses STE formation.[46] Conversely, $DPDAPbI_4$ shows a transient broadening and asymmetry at low compression consistent with the STE admixture, followed by recovery of a symmetric, FE-dominated profile as further pressure reduces octahedral distortion.[45] Across these DJ examples, PL enhancement at increasing pressure is primarily associated with the FE channel,[45] while STE features are typically stabilized only within a limited low-to-intermediate pressure window when tilting or interlayer misregistry is prominent—opposite to many RP cases where STE bands emerge and intensify at moderate pressures. This behavior is reflected in stronger through-layer connectivity in DJs (bifunctional spacers and robust hydrogen bonding) that constrains layer sliding and promotes pressure-induced delocalization, broadening the regime where FE emission outcompetes STE; at sufficiently high loads, however, accumulated disorder and non-radiative pathways ultimately quench luminescence. The precise crossover pressures remain spacer- and composition-dependent.[45,46]

4.5. Charge-carrier lifetimes: pressure as a trap suppressor

Pressure can also modulate charge-carrier lifetimes, which can be measured using time-resolved PL (TRPL) measurements, where carrier lifetimes typically increase as non-radiative pathways are eliminated under pressure and then collapse when amorphization or non-emissive transitions dominate. For example, Yin *et al.* found that in $(BA)_2PbI_4$, the lifetime increased from 150 to 190 ps upon compression to 0.4 GPa, with the STE (slow decay) lifetime undergoing a significant increase from 320 to 440 ps (Fig. 15a and b) attributed to an increase of trapped excitons by the distorted PbI_4^{2-} lattices.[21] Upon further compression to 2.3 GPa, the lifetime decreased to 53 ps with the STE lifetime decreasing to 148 ps (Fig. 15c) as non-radiative recombination increased resulting from increased defects due to the onset of amorphization.[21] Similarly, in $(2meptH_2)PbCl_4$

 This journal is © The Royal Society of Chemistry 2026

Open Access Article. Published on 28 Oktober 2025. Downloaded on 16.02.26 09:35:21.
This article is licensed under a Creative Commons Attribution-NonCommercial 3.0 Unported Licence.

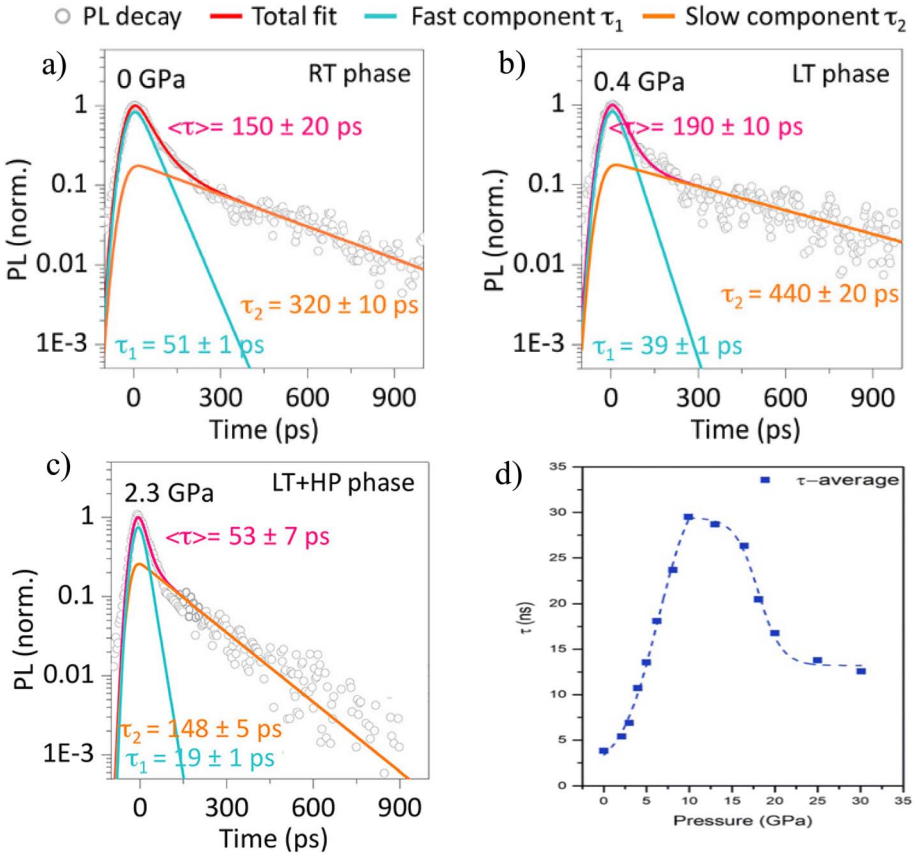

Fig. 15 Pressure-induced charge carrier lifetimes of 2D HOIPs. (a)–(c) TRPL spectra of $(BA)_2PbI_4$ at 0, 0.4, and 2.3 GPa, respectively. Reproduced from ref. 21 with permission from American Chemical Society, copyright 2018. (d) Average PL lifetime as a function of pressure of $(2meptH_2)PbCl_4$. Reproduced from ref. 34 with permission from the Royal Society of Chemistry, copyright 2023.

the average carrier lifetime exhibits a significant increase until 10.2 GPa, again associated with increased radiative recombination resulting in PL enhancement, followed by a gradual decrease, again associated with increased non-radiative recombination resulting in PL quenching (Fig. 15d).[34]

Furthermore, in certain cases, structural rearrangements persist after pressure release, resulting in metastable phases with enhanced optoelectronic properties. For example, structural amorphization upon compression followed by recrystallization upon decompression in $(BA)_2(MA)_2Pb_3I_{10}$ resulted in metastable states which exhibited a significant bandgap narrowing of 8.2%.[47] Metastable states have also been observed in GA-based compounds; for example in $(GA)(MA)_2Pb_2I_7$ decompression from 25.1 GPa resulted in a colour change from dark red to black and a bandgap decrease from 2.00 (pre-compression) to 1.79 eV (post-decompression), indicating irreversible pressure behavior ideal for practical applications.[50] In $(HA)_2(GA)Pb_2I_7$ decompression until 1.5 GPa results in significant PL enhancement *via* laser irradiation accompanied by a yellow to orange colour change which is retained at ambient pressure and exhibits a PL enhancement of 100% compared to the original pre-compressed sample.[53] These observations raise the possibility of using pressure not only as a diagnostic tool but also for post-synthetic phase engineering, whilst also suggesting a strategy for "strain-quenching" of pressure-induced states that could be useful for stabilizing materials for light emission or sensing.

Taken together, these results demonstrate that high pressure provides a robust route to tailor and even stabilize the optoelectronic properties of 2D HOIPs. The magnitude of modulation, reversibility, and emissive pathways depend strongly on dimensionality, spacer rigidity, interlayer coupling, and metal/halide identity. The strategic use of pressure can thus advance both the fundamental understanding and practical engineering of 2D perovskites. Table 2 summarizes the pressure-induced optoelectronic properties of representative 2D HOIPs.

This table collates optical and electronic responses (bandgap shifts and PL modulation) under hydrostatic compression. Several general trends are evident: (i) soft-spacer RP systems often display monotonic bandgap narrowing with pressure, (ii) rigid-spacer systems can show abnormal behaviors such as initial blueshift or non-monotonic shifts, and (iii) DJ systems exhibit gradual tuning due to stronger interlayer interactions. Photoluminescence (PL) is frequently enhanced at low pressure due to defect passivation, followed by quenching at higher pressures. Notably, broadband self-trapped exciton (STE) emission and direct-to-indirect bandgap transitions have been observed in select systems, highlighting pressure as a versatile tuning parameter.

Open Access Article. Published on 28 Oktober 2025. Downloaded on 16.02.26 09:35:21.
This article is licensed under a Creative Commons Attribution-NonCommercial 3.0 Unported Licence.

Table 2 Summary of high-pressure effects on optoelectronic properties of 2D hybrid perovskites

2D perovskite	Pressure range (GPa)	Pressure range of PL enhancement (GPa)	Bandgap modulation range (eV)	Pressure effects on optical properties[a]	Reversibility[b]	Ref.
$(PEA)_2PbI_4$	0–8	N/A	N/A direct–indirect transition at 5.8 GPa	PL: RS with CI → DI → quenching	PR (PL)	19
	0–7	N/A		PL: RS with DI of peak 1 (2.16 eV) → quenching; AE: RS → abrupt BS	PR (PL and BG)	51
$(PEA)_2PbBr_4$	0–48	N/A	2.99 → 2.35	PL: RS with DI → quenching; AE: RS → abrupt BS → re-RS; BG: BR → BW → BR	PR (PL) and IR (BG)	27
	0–30	4.0–8.0 (STE)	2.96 → 2.46	PL (FE): RS with DI → quenching; PL (STE at ~4 GPa) EI → DI → quenching; AE: RS → abrupt BS → re-RS; BG: BR → BW → BR	R (PL and BG)	52
$(PEA)_2PbCl_4$	0–30	0–0.4 (STE) and 2.1–4.6 (FE)	3.57 → 3.13	PL (STE): BS → RS; PL (FE): RS; PL (STE & FE): EI (5-fold) → DI → quenching; AE: RS → quenching; BG: significant BR	IR (PL and BG)	30
$(BA)_2PbI_4$	0–11	0.85–1.07; 3.09–8.7	N/A	PL(FE): RS → quenching; PL2: RS with EI → DI → quenching; PL3 (~3.10 GPa): → RS with EI → quenching	PR (PL)	20
	0–10	N/A	N/A	PL: all RS; AE: abrupt initial BS → RS	PR (PL)	21
	0–40	0–2.6 (PL 1)	2.28 → 0.95	PL1: abrupt initial BS → RS with EI → quenching; PL2: (at 2.6 GPa) → DI → quenching; PL3: (at 9.2 GPa) → quenching; AE: abrupt BS → RS; BG: BW → BR	R (BG) IR (PL and BG)	22
$(BA)_2(MA)Pb_2I_7$	0–10	N/A	N/A	PL1 & 2: RS → peaks merge → BS → quenching	R (PL)	37
$(BA)_2PbBr_4$	0–13	N/A	~2.5 → 1.8	PL and AE: RS; BG: significant BR	R (PL and BG)	26
	0–20	0–0.9 (FE) and 3.4–12.9 (STE)	~3.0 → 2.55	PL: RS with EI → broad-band emission at 3.4 GPa → coexistence of blue and broad-band emission; AE: RS → BS; BG: BR → BW	R (PL and BG)	28
$(BA)_2(MA)Pb_2Br_7$	0–15	N/A	~2.25 → 1.9	PL: RS→ BS with DI → quenching; AE: RS → BS; BG: BR → BW	R (PL and BG)	26
$(OA)_2PbI_4$	0–13	1.48–4.70 (PL2)	N/A	PL1 (FE): RS with DI → quenching; PL2 (~1.48 GPa) → EI → quenching	PR (PL)	20
$(DDA)_2PbI_4$	0–14	0.41–2.12 (PL3)	N/A	PL1(FE): RS with DI → quenching; PL2 (at 0.41 GPa): RS with DI → quenching; PL3 (at 0.41 GPa): RS with EI →DI → quenching; PL4 (at 1.79 GPa): RS → quenching	PR (PL)	20
ETA_2PbI_4	0–10	0–1.5	2.24 → 1.85	PL (FE): RS → 4-fold EI → DI → quenching; AE: RS; BG: significant BR	PR (PL)	23
$(4BrPhMA)_2PbBr_4$	0–2	N/A	N/A	PL: moderate RS with DI	PR (PL)	24
$(PMA)_2PbI_4$	0–20	N/A	2.19 → 1.26	RS of absorption edge → slight BS → re-RS; BG: significant BR → slight BW → BR	R (BG)	29

This journal is © The Royal Society of Chemistry 2026

Open Access Article. Published on 28 Oktober 2025. Downloaded on 16.02.26 09:35:21.
This article is licensed under a Creative Commons Attribution-NonCommercial 3.0 Unported Licence.

Table 2 (*Contd.*)

2D perovskite	Pressure range (GPa)	Pressure range of PL enhancement (GPa)	Bandgap modulation range (eV)	Pressure effects on optical properties[a]	Reversibility[b]	Ref.
$(GA)_2PbI_4$	0–15	N/A	2.55 → 2.33	PL: RS → BS → quenching; AE: RS → BS; BG: BR → BW	N/A	32
$(BzA)_2PbI_4$	0–0.35	N/A	2.36 → 2.327	PL: RS; AE: RS; BG: BR	R (PL and BG)	33
$(BzA)_2PbBr_4$	0–0.35	N/A	3.07 → 3.015	PL: RS; AE: RS; BG: BR	R (PL and BG)	33
$(MeOPEA)_2PbI_4$	0–7	N/A	N/A	PL: RS with CI	R (PL)	35
$(MeOPEA)_2PbBr_4$	0–8	N/A	N/A	PL: RS with CI	R (PL)	35
$(CMA)_2PbI_4$	0–15	0–0.8	2.33 → 1.89	PL(FE): RS with 10-fold EI → DI → quenching; AE: RS; BG: significant BR	R (PL and BG)	36
$[4MeOPEA]_2PbBr_4$	0–18	0–0.6 (STE) and 0.6–2.59 (FE)	N/A	PL (STE): BS with EI → DI → quenching; PL(FE at 0.60 GPa): RS with EI → DI → quenching	R (PL)	38
MHy_2PbI_4	0–7	~ 0–1.75	2.03 → 1.86	PL(FE): RS with EI → quenching; AE: RS; BG: substantial BR	R (PL and BG)	41
$(CHEA)_2PbI_4$	0–8	N/A	~2.4 → 2.0	PL: RS → BS with DI AE: RS → BS; significant BR → BW	R (PL and BG)	42
MHy_2PbBr_4	0–7	N/A	2.90 → 2.723	AE: RS; BG: BR → BW	R (BG)	43
	0–8	0.07–4.49	2.812 → 2.662	PL (FE): RS → BS with 11-fold EI → quenching; AE: RS → BS; BG: BR → BW	R (PL and BG)	55
$(C_7H_7N_2)_2PbBr_4$	0–17	0–3.5	2.775 → 2.25	PL (FE): RS with EI → DI → quenching; AE: RS → slight BS → re-RS; BG: BR → slight BW → BR	IR (PL and BG)	44
$(C_7H_7N_2)_2PbCl_4$	0–18	0–3.3 (FE) and 6–8.3 (broadband)	3.375 → 3.0	PL(STE): BS → quenching; PL(FE): RS with EI→ DI→ quenching; AE: RS → BS → re-RS; BG: BR → BW → BR	IR (PL and BG)	44
Tz_2PbBr_4	0–13	0–7.77	N/A	PL (FE and STE at 4.42 GPa): RS with EI → BS with DI → quenching	N/A	56
$(3AMP)PbI_4$	0–30	0–6	2.10 → 1.63	PL: Large RS with EI → DI; AE: RS → BS → re-RS; BG: BR → BW → BR	IR (PL and BG)	25
$(3AMP)(MA)Pb_2I_7$	0–30	N/A	1.85 → 1.6	AE: RS → BS → re-RS; BG: BR → BW → BR	IR (BG)	25
S-$[4APEA]PbI_4$	0–12	N/A	N/A	PL: RS with DI → quenching	PR (PL)	31
$(PDMA)PbI_4$	0–0.35	N/A	2.41 → 2.383	PL and AE: RS; BG: BR	R (PL and BG)	33
$(PDMA)PbBr_4$	0–0.35	N/A	3.06 → 3.029	PL and AE: RS; BG: BR	R (PL and BG)	33
$(2meptH_2)PbCl_4$	0–30	1.5–9.9	3.55 → 3.32	PL: BS with 8-fold EI → RS and DI → quenching; AE: RS → BS → RS; BG: BR → BW → BR	N/A	34
$IMMHyPbBr_4$	0–10	~0–2	N/A	PL (FE): RS with EI → DI	R (PL)	40
$(API)PbBr_4$	0–6	0–2.7	~3.1 → 2.75	PL(STE): BS with DI → quenching; PL (new FE): BS with EI →DI; AE: RS; BG: significant BR	R (BG)	46
$DPDAPbI_4$	0–9	0–1.49	2.26 → 1.87	PL (FE): RS with EI → DI → quenching; AE: RS; BG: significant BR	R (PL and BG)	45
$(GA)(MA)_2Pb_2I_7$	0–25	0–1.3	2.00 → 1.52	PL: RS with 5-fold EI → quenching; AE: RS→BS→RS; BG: BR → BW → BR	IR (PL and BG)	50

Open Access Article. Published on 28 Oktober 2025. Downloaded on 16.02.26 09:35:21.
This article is licensed under a Creative Commons Attribution-NonCommercial 3.0 Unported Licence.

Table 2 (*Contd.*)

2D perovskite	Pressure range (GPa)	Pressure range of PL enhancement (GPa)	Bandgap modulation range (eV)	Pressure effects on optical properties[a]	Reversibility[b]	Ref.
$(HA)_2(GA)Pb_2I_7$	0–9	0–1.59	~2.14 → 1.8	PL (FE): RS with 12-fold EI → DI → quenching; AE: RS → BS → RS; BG: BR → BW → BR	R (PL) and IR (BG)	53
$(BA)_2(GA)Pb_2I_7$	0–5	0–2.1	2.21 → 1.91	PL(FE): RS with 72-fold EI → DI; AE: RS → quenching; BG: BR	N/A	39

[a] RS = redshift; BS = blueshift; CI = constant intensity; DI = decreasing intensity; EI = enhancing intensity FE = free exciton; STE = self-trapped exciton; AE = absorption edge; BG = bandgap; BR = bandgap reduction; BW = bandgap widening. [b] R = reversible; IR = irreversible; PR = partially reversible.

5. Lead *vs.* lead-free: contrasting pressure responses

Two-dimensional (2D) perovskites based on lead halides have been extensively studied for their superior optoelectronic properties and tunability under hydrostatic pressure. However, the toxic nature of Pb^{2+} and associated environmental concerns have motivated the development of lead-free alternatives. This section summarizes the pressure behavior of lead-free 2D perovskites, including Sn^{2+}, Cu^{2+}, Ge^{2+}, and Bi^{3+} analogs, in terms of structural stability, bandgap evolution, PL response, and phase transition mechanisms.

A key advantage of lead-free 2D perovskites, in particular Sn^{2+} and Cu^{2+}-based ones, is the narrow bandgaps which allow for greater tuning under high pressure allowing for greater possibility for reaching the ideal Shockley–Queisser (SQ) limit, which states that at an optimal bandgap of 1.34 eV a maximum efficiency of 33.7% is achieved.[67,68] Unfortunately, lead-free analogs often exhibit greater susceptibility to oxidation (*e.g.*, $Sn^{2+} \rightarrow Sn^{4+}$), which can influence their high-pressure behavior and long-term stability. Despite this, certain Sn and Cu-based systems have demonstrated similar or even enhanced phase transition pathways, PL enhancements, and bandgap shifts in comparison to their lead-based analogues. Bi^{3+}-based 2D perovskites, with their larger tolerance for structural distortion, typically show broader bandgaps and more rigid frameworks, resulting in less pronounced PL modulation under pressure. Overall, while lead-free systems offer promising environmental advantages, their pressure responses are often more limited or require additional chemical tuning to match the performance and versatility of their lead-based counterparts.

5.1. Tin-based systems: high tunability but oxidation challenges

Sn^{2+} is believed to be the most promising substitute for lead in the generation of 2D HOIPs owing to the highly favourable optical and electronic properties of Sn^{2+}-based 2D HOIPs.[69] In particular, Sn^{2+}-based 2D HOIPs with optical bandgaps between 1.2–1.4 eV have the potential to reach a power conversion efficiency (PCE) of around 33%.[70] Furthermore, they also tend to exhibit similar or enhanced optical and electronic properties in comparison to their Pb-based analogues, including greater charge carrier mobilities and long-lived hot carriers.[69,71,72] Unfortunately Sn^{2+}-based 2D HOIPs suffer from lower chemical stability with Sn^{2+} readily oxidizing to Sn^{4+} under ambient conditions,[73] leading to poor reproducibility and efficiency and large doping concentrations.[74] Furthermore, high-pressure studies of Sn^{2+}-based 2D HOIPs are very limited. A recent study by Kong *et al.* on an RP-type family, $(BA)_2(MA)_{n-1}Sn_nI_{3n+1}$ ($n = 2$–4), showed a significant bandgap reduction for the $n = 2$ sample from 1.65 to 1.17 eV upon compression to 6.2 GPa and significant enhancement of PL intensity until 1 GPa followed by a significant decrease and eventual quenching at 6.5 GPa (Fig. 16).[75] Interestingly, all three samples exhibited similar patterns for both the PL emission and bandgap, with the PL intensity enhancing at low pressure before reducing and the bandgap exhibiting a significant redshift before a slight

This journal is © The Royal Society of Chemistry 2026

Open Access Article. Published on 28 Oktober 2025. Downloaded on 16.02.26 09:35:21.
This article is licensed under a Creative Commons Attribution-NonCommercial 3.0 Unported Licence.

blueshift and re-redshift at high pressure (Fig. 16).[75] Furthermore, the $n = 2$ sample exhibited the greatest bandgap tunability ($\Delta E_g = 0.48$ eV), much greater compared to that of the lead analogue ($\Delta E_g = 0.15$ eV), and lowest bulk modulus of 4.8 GPa indicating significant compressibility compared to its 3D Sn and 2D Pb counterparts.[75] The bandgap and crystalline structure of the $n = 2$ sample were also found to be retained upon decompression from mild pressures.[75] This recent study underlines the strong possibility of Sn^{2+}-based 2D HOIPs for achieving the desired SQ limit with considerable compressibility in comparison to the lead analogues. However, the limited high-pressure studies open the door for more extensive studies to be conducted to fully understand the effects of high pressure on the structures and tuning of optoelectronic properties of Sn^{2+}-based 2D HOIPs. These findings highlight the potential of Sn^{2+}-based 2D HOIPs as viable alternatives for environmentally friendly optoelectronic applications—provided that oxidative degradation can be effectively mitigated. Continued advancements in encapsulation strategies and inert-atmosphere processing will be key to unlocking the full promise of these materials in high-pressure regimes.

5.2. Copper-based systems: stability with narrow bandgaps

Another commonly studied alternative to lead in 2D HOIPs is copper, specifically Cu^{2+}, which has emerged as a highly promising candidate due to its abundance, low cost, and low environmental impact and the unique electronic structure and excellent optoelectronic properties of Cu^{2+}-based 2D HOIPs.[76,77] In contrast to tin, copper-based 2D HOIPs exhibit excellent stability mostly due to the use of hydrophobic organic cations as spacers in between the inorganic layers, making them more moisture resistant in comparison to unstable 3D perovskites, and they are also less susceptible to oxidation under ambient conditions.[77,78] The majority of Cu^{2+}-based 2D HOIPs consist of Cu–Br or Cu–Cl octahedra, with Cu–Cl ones known for

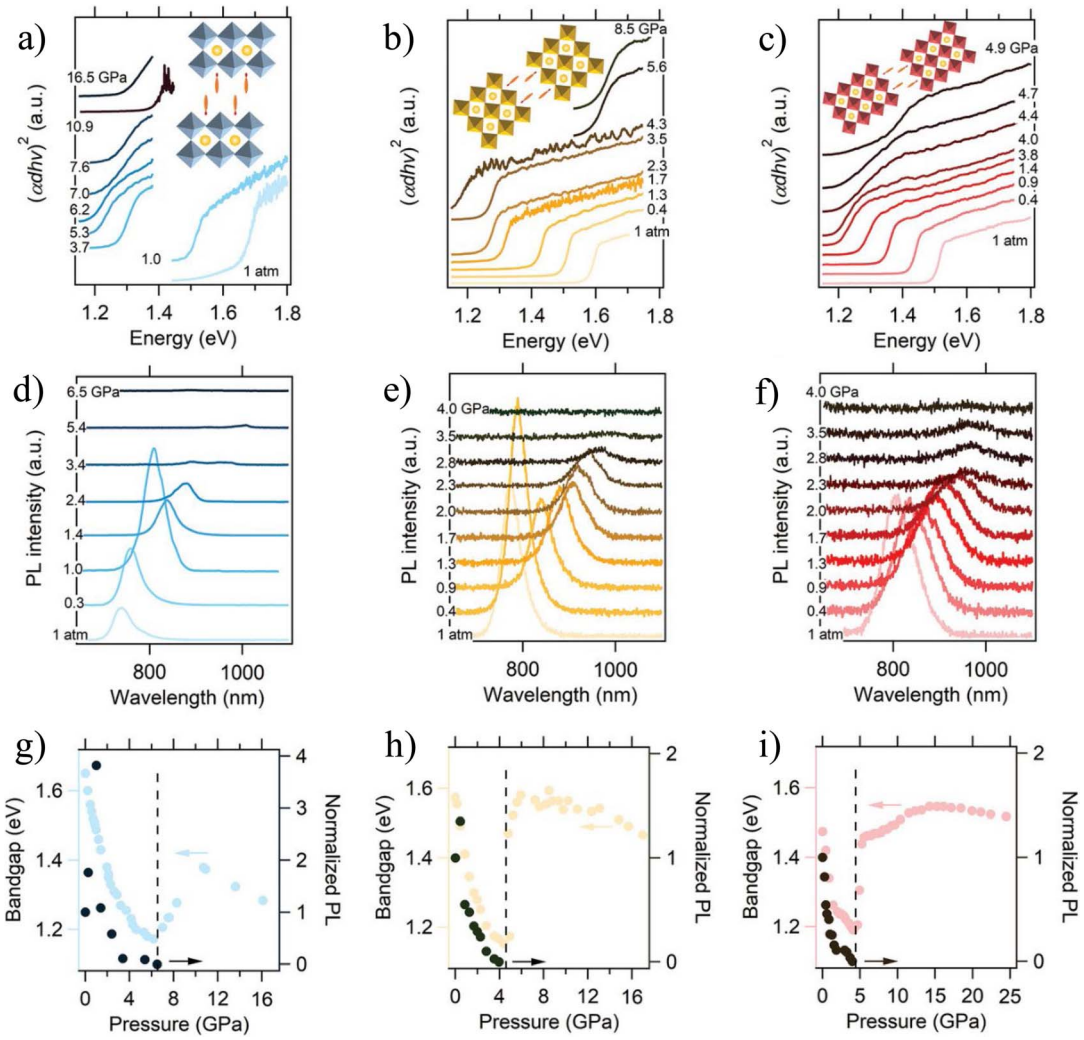

Fig. 16 Tuning of optoelectronic properties of the $(BA)_2(MA)_{n-1}Sn_nI_{3n+1}$ RP family. Absorption spectra upon compression for (a) $(BA)_2(MA)Sn_2I_7$, (b) $(BA)_2(MA)_2Sn_3I_{10}$, and (c) $(BA)_2(MA)_3Sn_4I_{13}$. PL spectra upon compression for (d) $(BA)_2(MA)Sn_2I_7$, (e) $(BA)_2(MA)_2Sn_3I_{10}$, and (f) $(BA)_2(MA)_3Sn_4I_{13}$. Bandgap as a function of pressure for (g) $(BA)_2(MA)Sn_2I_7$, (h) $(BA)_2(MA)_2Sn_3I_{10}$, and (i) $(BA)_2(MA)_3Sn_4I_{13}$. Reproduced from ref. 75 with permission from Wiley-VCH GmbH, copyright 2024.

Open Access Article. Published on 28 Oktober 2025. Downloaded on 16.02.26 09:35:21.
This article is licensed under a Creative Commons Attribution-NonCommercial 3.0 Unported Licence.

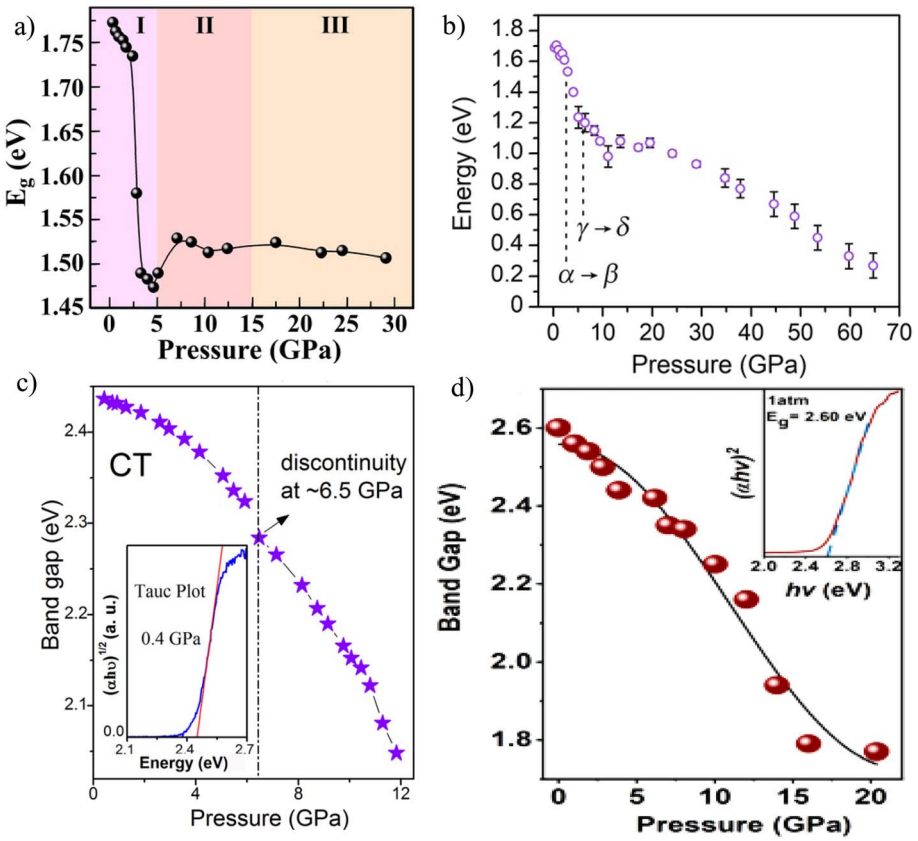

Fig. 17 Pressure-induced bandgap behavior of Cu-based 2D HOIPs. (a) Bandgap as a function of pressure for $(PMA)_2CuBr_4$. Reproduced from ref. 79 with permission from Wiley-VCH GmbH, copyright 2022. (b) Bandgap as a function of pressure for $(EA)_2CuBr_4$. Reproduced from ref. 80 with permission from Wiley-VCH GmbH, copyright 2019. (c) Bandgap as a function of pressure for $DABCuCl_4$. Reproduced from ref. 81 with permission from American Chemical Society, copyright 2017. (d) Bandgap as a function of pressure for $(PEA)_2CuCl_4$. Reproduced from ref. 82 with permission from American Physical Society, copyright 2023.

exhibiting thermochromism resulting from the lattice undergoing phase transitions resulting from temperature-dependent hydrogen bonding of cations.[77,78] More extensive high-pressure studies have been conducted on Cu^{2+}-based 2D HOIPs compared to Sn^{2+}-based ones, with those containing Cu–Br octahedra exhibiting greater potential for achieving the SQ limit compared to those with Cu–Cl octahedra due to the narrow bandgaps at ambient pressure. For example, Zahn *et al.* observed a significant bandgap reduction from 1.8 to 1.47 eV upon compression to 5 GPa (Fig. 17a) in $(PMA)_2CuBr_4$ resulting from the deformation of the Cu–Br octahedra due to rapid compression of the volume, but no significant phase transition.[79] Compression beyond 5 GPa results in a slight blueshift of the bandgap to 1.52 eV, attributed to pressure-induced tilting of the Cu–Br octahedron, after which the bandgap remains stable and at 1.52 eV up to 29.1 GPa (Fig. 17a), which is highly favourable for photovoltaic devices.[79] Similarly, Jaffe *et al.* observed a large bandgap reduction from 1.7 to 0.3 eV in $(EA)_2CuBr_4$ upon compression to 65 GPa (Fig. 17b).[80] In contrast to $(PMA)_2CuBr_4$, $(EA)_2CuBr_4$ undergoes two distinct phase transitions, first from the monoclinic $P2_1/c$ structure at ambient pressure to orthorhombic *Cccm* upon compression to 2.6 GPa, resulting in octahedral tilting, followed by a second-order isostructural phase transition above 4 GPa, resulting in reduced compressibility.[80] Li *et al.* also observed a substantial bandgap reduction in $DABCuCl_4$ from 2.44 to 2.05 eV upon compression to ~12 GPa along with an isostructural phase transition between ~6 and ~10 GPa (Fig. 17c).[81] Zhou *et al.* observed an even greater bandgap reduction in $(PEA)_2CuCl_4$ from 2.93 to 1.77 eV upon compression to 20.37 GPa (Fig. 17d), but similar to $(PMA)_2CuBr_4$ no significant phase transition was observed.[82] These findings help underline the greater probability for achieving the desired SQ limit in Cu–Br 2D HOIPs in comparison to Cu–Cl 2D HOIPs, and the lack of oxidation under ambient conditions and excellent stability make Cu^{2+} a highly promising candidate to replace lead but further studies are likely required to deepen the understanding of both the structural evolution and bandgap behaviour under high pressure.

5.3. Germanium-based systems: underexplored but promising

In contrast to tin and copper, germanium (Ge^{2+}) has been studied far less as a potential alternative to lead mainly due to its rare abundance and high cost. However, germanium exhibits little toxicity and environmental damage in comparison to lead and a growing interest in Ge^{2+}-based 2D HOIPs for various applications is anticipated in the coming years.[83] Unfortunately, like Sn^{2+} Ge^{2+} also shows a strong tendency to oxidize to Ge^{4+}

 This journal is © The Royal Society of Chemistry 2026

Open Access Article. Published on 28 Oktober 2025. Downloaded on 16.02.26 09:35:21.
This article is licensed under a Creative Commons Attribution-NonCommercial 3.0 Unported Licence.

under ambient conditions, but the majority of the solutions to suppress the oxidation proposed for Sn^{2+} can also be applied to Ge^{2+}.[83] Furthermore, high-pressure studies on Ge^{2+}-based 2D HOIPs are also highly scarce. In 2021 Morana *et al.* observed a reversible broadband PL peak in $(DA)_2GeI_4$ upon compression beyond 2.1 GPa, which reaches its maximum intensity at around 3.7 GPa (Fig. 18a), likely resulting from STE emission due to octahedral distortion.[84] An initial blueshift of the absorption edge is observed upon compression to 0.2 GPa followed by a continuous redshift until 11.4 GPa leading to a significant reduction of the absorption edge from 2.28 to 1.64 eV (Fig. 18b).[84] The onset of both the broadband PL emission and bandgap blueshift–redshift transition correlate excellently with the proposed phase transition from orthorhombic *Pbca* to monoclinic $P2_1/a$ with a reduced *c*-axis between 0.56 and 2.20 GPa, evidenced by peak splitting in the XRD spectra at 2.20 GPa (Fig. 18c) and discontinuity of the unit cell parameters at around 0.56 GPa (Fig. 18d).[84] Overall, this study once again indicates the strong probability for reaching the SQ limit in lead-free 2D HOIPs; however, furthermore, more in-depth studies are required to obtain a more solid foundation of the pressure response of Ge^{2+}-based 2D HOIPs.

5.4. Bismuth-based systems: robust but optically limited

Lastly, Bi^{3+}-based double perovskites and layered compounds represent another lead-free direction. These systems are generally more rigid and exhibit wider, often indirect bandgaps. Under pressure, Bi-based compounds show mild bandgap narrowing, but less pronounced structural phase transitions compared to Pb or Sn systems.[54,85,86] For example, $MA_3Bi_2Br_9$ exhibited a phase transition between 4.3 and 5.0 GPa from trigonal $P\bar{3}m1$ to monoclinic $P2_1/a$ evidenced by the emergence of new peaks in the XRD spectra (Fig. 19a).[85] A continuous redshift of the absorption edge (Fig. 19b), resulting in a mild

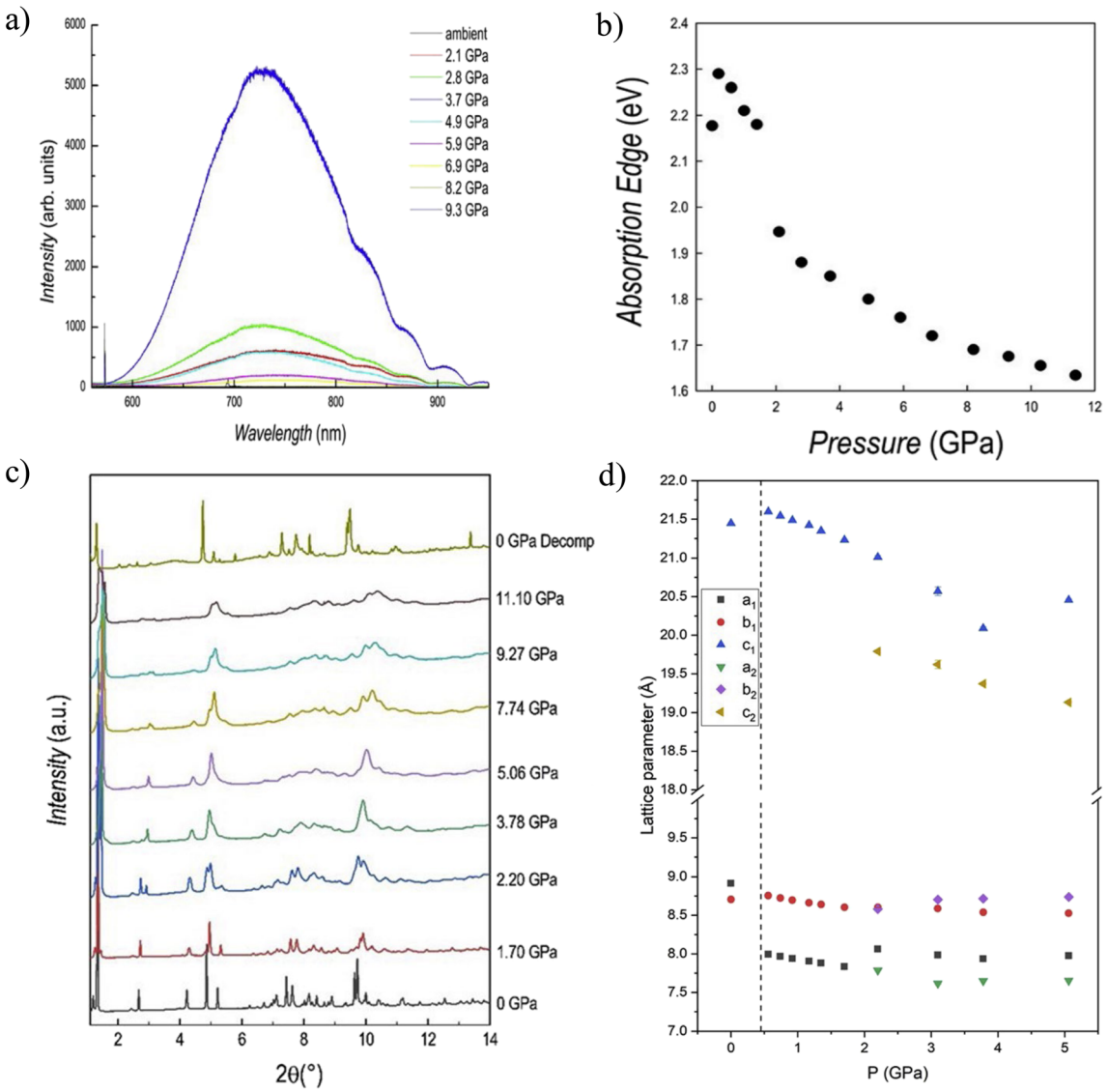

Fig. 18 Behavior of $(DA)_2GeI_4$ under high pressure. (a) PL spectra upon compression, (b) absorption edge as a function of pressure, (c) XRD spectra upon compression, and (d) unit cell parameters as functions of pressure. Reproduced from ref. 84 with permission from Elsevier, copyright 2022.

Open Access Article. Published on 28 Oktober 2025. Downloaded on 16.02.26 09:35:21.
This article is licensed under a Creative Commons Attribution-NonCommercial 3.0 Unported Licence.

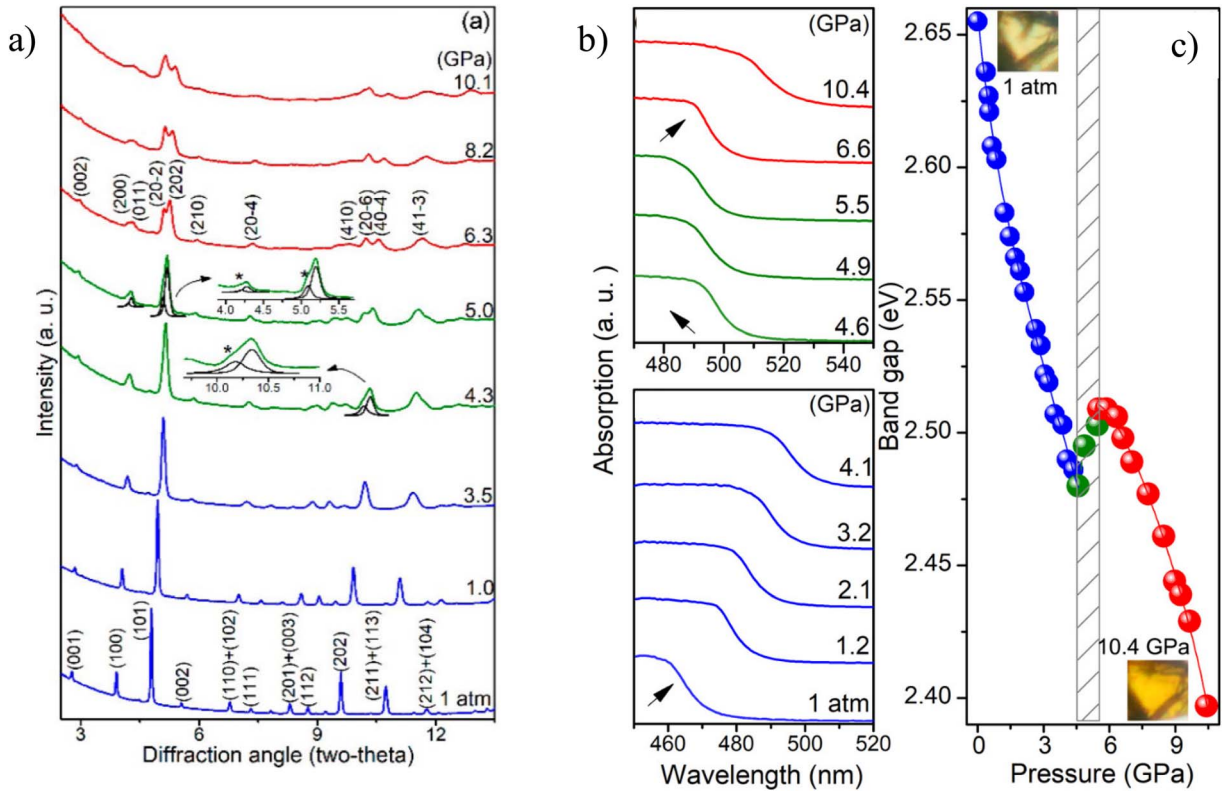

Fig. 19 Behavior of $MA_3Bi_2Br_9$ under high pressure. (a) ADXRD spectra upon compression, (b) UV-vis absorption spectra upon compression, and (c) bandgap as a function of pressure. Reproduced from ref. 85 with permission from American Chemical Society, copyright 2019.

bandgap reduction of ~0.2 eV (Fig. 19c), upon compression to 4.1 GPa was observed followed by a slight blueshift between 4.6 and 5.5 GPa and finally a re-redshift upon further compression to 10.4 GPa (Fig. 19b), resulting in another mild bandgap reduction of ~0.1 eV (Fig. 19c).[85] In comparison, $Cs_3Bi_2I_6Cl_3$ was found to exhibit a near constant bandgap upon compression to 13.6 GPa, followed by a gradual redshift, and no significant phase transition.[86] Furthermore, the PL response in Bi perovskites is often weak and pressure-insensitive, though certain mixed-halide Bi compounds have shown slight activation under compression.[86] For instance, a sharp increase in the PL intensity until 13.4 GPa was observed in the mixed-halide $Cs_3Bi_2I_6Cl_3$.[86] The 6 s^2 lone pair of Bi^{3+} contributes to local structural distortion, but its stereochemical activity is less pronounced than in Sn^{2+} or Pb^{2+}, resulting in reduced exciton localization and diminished light emission under pressure. As a result, Bi^{3+}-based 2D perovskites may be more suited for applications requiring structural robustness and environmental stability rather than dynamic optoelectronic tunability. Nonetheless, ongoing efforts to enhance their emissive properties through halide alloying, organic spacer modification, and external stimuli like pressure continue to expand the design space for stable, lead-free perovskite materials.

Sn^{2+}-based compounds offer good compressibility and bandgap tunability but suffer from oxidation. Cu^{2+} systems offer similar properties to Sn^{2+} systems with the added bonus of reduced oxidation, but Cu–Cl systems exhibit wider bandgaps and thus a lower probability for reaching the desired SQ limit. Ge^{2+} systems are also less prone to redox instability but require pressure to activate their emissive states. Bi^{3+} perovskites are structurally robust but have limited optical responsiveness. Despite these differences, all four lead-free systems benefit from pressure-tuning as a non-invasive method to modulate properties, access metastable phases, or suppress defects. For example, pressure-cycled $(DA)_2GeI_4$ retained broadband emission even after decompression,[84] while stabilized Sn^{2+} systems retained narrowed bandgaps post-pressure.[75] These results underscore the importance of integrating high-pressure studies into the evaluation of next-generation lead-free perovskites. Table 3 summarizes structural, optical, and reversibility trends observed under pressure across Pb^{2+} Sn^{2+}, Cu^{2+}, Ge^{2+}, and Bi^{3+}-based 2D HOIPs.

This table contrasts the high-pressure responses of Pb-based 2D HOIPs with those of Sn, Cu, Ge, and Bi analogues. Pb-based systems exhibit rich polymorphism and strong bandgap tunability but raise toxicity concerns. Sn-based systems display even greater bandgap shifts and compressibility, though they suffer from oxidation instability. Cu-based systems (especially Cu–Br) combine tunability with greater environmental stability, whereas Cu–Cl analogues have wider bandgaps and limited photovoltaic relevance. Ge-based systems are underexplored but show promising pressure-activated photoluminescence and significant bandgap narrowing. Bi-based layered perovskites are structurally robust with only mild optical responses. Taken together, these comparisons underscore the potential of pressure as a universal tool for accessing metastable phases and tailoring properties in both lead and lead-free 2D HOIPs.

This journal is © The Royal Society of Chemistry 2026

Open Access Article. Published on 28 Oktober 2025. Downloaded on 16.02.26 09:35:21.
This article is licensed under a Creative Commons Attribution-NonCommercial 3.0 Unported Licence.

Table 3 Comparison of high-pressure behavior between lead-based and lead-free 2D perovskites[a]

Property	Lead-based (Pb^{2+}) and *Lead-free (Sn^{2+}, Cu^{2+}, Ge^{2+}, and Bi^{3+})*	Representative examples with references
Bandgap	(1) Redshift and bandgap reduction	(1) ETA_2PbI_4 (ref. 23), $(Bz)_2PbI_4$ (ref. 33), $(Bz)_2PbBr_4$ (ref. 33), (PDMA)$PbBr_4$ (ref. 33), $(CMA)_2PbI_4$ (ref. 36), and $DPDAPbI_4$ (ref. 45)
	(2) Redshift → blueshift	(2) $(BA)_2(MA)Pb_2Br_7$ (ref. 26), $(GA)_2PbI_4$ (ref. 32), and MHy_2PbBr_4 (ref. 43 and 55)
	(3) Initial blueshift → redshift	(3) $(BA)_2PbI_4$ (ref. 22)
	(4) Initial redshift → abrupt blueshift → re-redshift	(4) $(3AMP)PbI_4$ (ref. 25), $(3AMP)(MA)Pb_2I_7$ (ref. 25), $(PEA)_2PbBr_4$ (ref. 27 and 52), $(PMA)_2PbI_4$ (ref. 29), $(GA)(MA)_2Pb_2I_7$ (ref. 50), and $(HA)_2(GA)Pb_2I_7$ (ref. 53)
	Redshift (Sn^{2+}, Cu^{2+}, and Ge^{2+}); stable or weak shift (Bi^{3+})	*$(BA)_2(MA)Sn_2I_7$(ref. 75), $(PMA)_2CuBr_4$(ref. 79), $(EA)_2CuBr_4$(ref. 80), $DABCuCl_4$(ref. 81), $(PEA)_2CuCl_4$(ref. 82), $(DA)_2GeI_4$(ref. 84), $Cs_3Bi_2Br_9$(ref. 54), $MA_3Bi_2Br_9$(ref. 85),* and *$Cs_3Bi_2I_6Cl_3$(ref. 86)*
Photoluminescence	(1) Gradual decrease → quenching	(1) $(PEA)_2PbI_4$ (ref. 19 and 51), $(BA)_2(MA)Pb_2Br_7$ (ref. 26), *S*-[4APEA]PbI_4 (ref. 31), and $(BA)_2(MA)Pb_2I_7$ (ref. 37)
	(2) Initial enhancement → gradual reduction → quenching	(2) $(BA)_2PbI_4$ (ref. 20 and 22), ETA_2PbI_4 (ref. 23), $(CMA)_2PbI_4$ (ref. 36), and $DPDAPbI_4$ (ref. 45)
	STE activation in Ge^{2+}; weak in Bi^{3+}	*$(DA)_2GeI_4$(ref. 84)* and *$Cs_3Bi_2I_6Cl_3$(ref. 86)*
Compressibility	High (smaller B_0)	$(BA)_2PbI_4$ (ref. 20–22) and $(CMA)_2PbI_4$ (ref. 36)
	Sn^{2+} and *Ge^{2+}: comparable Bi^{3+}: lower*	*$(BA)_2(MA)Sn_2I_7$(ref. 75), $(DA)_2GeI_4$(ref. 84),*and *$MA_3Bi_2Br_9$(ref. 85)*
Phase transitions	Multiple and often reversible	$(PEA)_2PbI_4$ (ref. 19 and 51), $(BA)_2PbI_4$ (ref. 20–22), $(PMA)_2PbI_4$ (ref. 29), and Tz_2PbI_4 (ref. 56)
	Fewer in Sn^{2+}, Cu^{2+}, and *Ge^{2+}; less pronounced in Bi^{3+}*	*$(BA)_2(MA)Sn_2I_7$(ref. 75), $(EA)_2CuBr_4$(ref. 80), $DABCuCl_4$(ref. 81), $(DA)_2GeI_4$(ref. 84),*and*$MA_3Bi_2Br_9$(ref. 85)*
Metastability	Observed in select compositions	$(GA)(MA)_2Pb_2I_7$ (ref. 50) and $(HA)_2(GA)Pb_2I_7$ (ref. 53)
	*In Sn^{2+}*and*Ge^{2+}only*	*$(BA)_2(MA)Sn_2I_7$(ref. 75)*and *$(DA)_2GeI_4$(ref. 84)*
PL persistence post-compression	Common	$(PEA)_2PbI_4$ (ref. 19 and 51), $(CMA)_2PbI_4$ (ref. 36), and $DPDAPbI_4$ (ref. 45)
	In Ge^{2+}; rare in Bi^{3+}	*$(DA)_2GeI_4$(ref. 84)*

[a] Lead-based are in normal font and lead-free are in italics.

6. Perspectives and outlook: pressure as a materials design tool

6.1. Conclusions

High-pressure research has opened a genuinely new control axis for 2D hybrid perovskites (2D HOIPs). Unlike chemical substitution, pressure enables continuous and reversible tuning of interlayer spacing, bond angles, and orbital overlap, thereby reshaping band structures and excitonic landscapes at will. In both Ruddlesden–Popper (RP) and Dion–Jacobson (DJ) phases, compression drives a spectrum of structural responses—from subtle order–disorder rearrangements to sequential polymorphic transitions and, at higher loads, amorphization—each with distinct optoelectronic signatures. This direct structure–property leverage has already yielded robust demonstrations of bandgap modulation (red/blue shifts), exciton conversion (FE↔STE), photoluminescence (PL) enhancement, and even rare elastic responses such as negative linear compressibility (NLC) in soft-spacer systems, together with metastable-state retention upon decompression that preserves desirable properties for device-relevant conditions.

A central, unifying insight is the role of spacer chemistry. Soft, van-der-Waals-separated RP systems (*e.g.*, BA and CMA) accommodate layer sliding/tilting and often show gradual, reversible tuning with pressure, while rigid, H-bond-connected DJ frameworks favor more abrupt or isostructural transitions and can quench PL when distortion pathways dominate. This RP–DJ contrast maps cleanly onto optical behavior—RP materials frequently show pressure-enhanced PL or reversible emission shifts; DJ analogues more often exhibit spectral abruptness and quenching—providing practical design rules for pressure-tolerant emitters and detectors.

Beyond acting as a diagnostic probe, pressure also serves as a synthetic handle. Several RP systems (*e.g.*, PEA/Br, MHy/Br, and triazolium/Br) demonstrate pressure-activated broadband emission *via* self-trapped excitons; lead-free analogues such as $(DA)_2GeI_4$ and tin-based RP families show strong bandgap tunability and, in some cases, post-pressure retention of narrowed gaps or broadband PL. These case studies illustrate the potential of compression to discover and then "lock in" hidden phases and emissive states that are difficult to access under ambient conditions through chemistry alone.

Finally, the lead-free landscape is converging with the pressure toolbox. Sn^{2+} systems offer large tunability but face oxidation; Cu^{2+} (especially Cu–Br) combines stability with promising gaps; Ge^{2+} remains underexplored yet exhibits pressure-activated emission; Bi^{3+} frameworks are robust but optically conservative. Taken

Open Access Article. Published on 28 Oktober 2025. Downloaded on 16.02.26 09:35:21.
This article is licensed under a Creative Commons Attribution-NonCommercial 3.0 Unported Licence.

together, these advances establish pressure as a universal, non-invasive route to compare, tune, and stabilize both Pb- and Pb-free chemistries toward environmentally responsible optoelectronics. Collectively, they underscore the emerging role of pressure as a true materials-design parameter for 2D HOIPs—one that complements composition and dimensionality to expand the accessible property space for adaptive photonics, sensing, and energy devices.

6.2. Outlook

Building on these advances, several directions can guide the next stage of progress:

• Quantitative structure–property maps under true hydrostatic conditions.

Many reported anomalies (*e.g.*, blueshift → redshift crossovers and non-monotonic trends) hinge on subtle balances between octahedral tilting and bond contraction, which are sensitive to pressure media and gradients. A priority is standardized hydrostatic protocols (medium choice, loading, and calibration) paired with parameterized descriptors (Pb–X–Pb angles and axial/equatorial bond compressibilities) to enable cross-study comparability and predictive design.

• Correlative, time-resolved *in situ* measurements.

Linking phase transitions to optical responses demands synchronized ADXRD/Raman/FTIR with PL/UV-vis in the same DAC and at identical pressure points. Adding TRPL will quantify trap suppression *vs.* STE formation kinetics; combined with variable-temperature and decompression cycles, this will separate reversible tuning from metastable trapping with device relevance.

• Metastable-state engineering ("pressure-quench" pathways).

Several systems retain narrower bandgaps or enhanced PL after pressure release, suggesting pathways to strain-lock useful states. Systematic maps of load-hold-release protocols (rates, dwell times, and partial unloads) could turn pressure into a post-synthetic step akin to annealing—particularly attractive for broadband emitters and near-ideal bandgaps in lead-free families. Additionally, pressure-induced compaction of interlayer spacing could offer practical stability benefits by limiting diffusion pathways for moisture ingress — a concept supported by studies on DJ-phase perovskites, where tighter interlayer connectivity is known to enhance humidity resistance. This suggests that pressure tuning may not only unlock new optical states but also passively improve environmental durability.

• Spacer-directed mechanics: designing softness *vs.* rigidity.

The RP–DJ divide is a design lever. Soft spacers (*e.g.*, aliphatic and cyclic) favor large, smooth tunability (and phenomena like NLC), while rigid, bifunctional spacers (DJ) enforce connectivity that can stabilize or sharply redirect transitions. Rational spacer engineering—including π-rigid, H-bonding, or ionic crosslinks—should target predictable compressibility and desired PL pathways (FE *vs.* STE).

• Lead-free platforms with pressure-assisted stabilization.

A particularly urgent frontier is the stabilization of Pb-free perovskites under pressure. For Sn-based systems, combining hydrostatic compression with tight redox control and mapping retention windows could turn transient narrowing into usable states. Pressure can also serve as a rapid screening tool, linking compressibility descriptors with tunability and persistence to identify promising compositions. Beyond Sn, Cu–Br compounds and emerging Ag–Bi/Sb layered analogues deserve exploration as intrinsically more stable and environmentally benign candidates, with pressure guiding their optimization and eventual integration into devices.

• Theory/simulation/ML: closing the experiment-theory loop.

First-principles calculations should be used to deconvolute angle *vs.* bond-length contributions to band dispersion under pressure. Building open datasets that connect pressure, structure, and optical properties for representative RP/DJ chemistries will enable machine learning models to predict critical pressures, phase sequences, STE onsets, and retention windows. Tight closed-loop workflows—where theory guides experimental pressure ranges and experiments iteratively refine models—will accelerate discovery and deliver prescriptive design rules for pressure-responsive, lead-free 2D perovskites.

Author contributions

Aditya Kutty: methodology, formal analysis, investigation, writing – original draft, review & editing, Yang Song: conceptualization, methodology, formal analysis, investigation, writing – review & editing, supervision, funding acquisition.

Conflicts of interest

There are no conflicts of interest to declare.

Data availability

No new data were generated in support of this review.

Acknowledgements

This work was supported by a Discovery Grant (RGPIN-2020-06422) and an Alliance International Catalyst Quantum Grant (ALLRP-580885-2022) from the Natural Science and Engineering Research Council of Canada.

References

1 A. K. Jena, A. Kulkarni and T. Miyasaka, *Chem. Rev.*, 2019, **119**, 3036–3103.
2 P. Roy, A. Ghosh, F. Barclay, A. Khare and E. Cuce, *Coatings*, 2022, **12**, 1089.
3 R. Sharif, A. Khalid, S. W. Ahmad, A. Rehman, H. G. Qutab, H. H. Akhtar, K. Mahmood, S. Afzal and F. A. Saleem, *Nanoscale Adv.*, 2023, **5**, 3803–3833.
4 R. A. Afre and D. Pugliese, *Micromachines*, 2024, **15**, 192.
5 B. Saparov and D. B. Mitzi, *Chem. Rev.*, 2016, **116**, 4558–4596.
6 L. Mao, C. C. Stoumpos and M. G. Kanatzidis, *J. Am. Chem. Soc.*, 2019, **141**, 1171–1190.
7 W. Fu, C. Pan, A. Zhou, P. Shi, Z. Yi and Q. Zeng, *Materials*, 2024, **17**, 6284.

 This journal is © The Royal Society of Chemistry 2026

Open Access Article. Published on 28 Oktober 2025. Downloaded on 16.02.26 09:35:21.
This article is licensed under a Creative Commons Attribution-NonCommercial 3.0 Unported Licence.

8 S. Li, Y. Jiang, J. Xu, D. Wang, Z. Ding, T. Zhu, B. Chen, Y. Yang, M. Wei, R. Guo, Y. Hou, Y. Chen, C. Sun, K. Wei, S. M. H. Qaid, H. Lu, H. Tan, D. Di, J. Chen, M. Grätzel, E. H. Sargent and M. Yuan, *Nature*, 2024, **635**, 82–88.
9 J. Guo, B. Wang, D. Lu, T. Wang, T. Liu, R. Wang, X. Dong, T. Zhou, N. Zheng, Q. Fu, Q, Z. Xie, X. Wan, G. Xing, Y. Chen and Y. Liu, *Adv. Mater.*, 2023, **35**, 2212126.
10 M. Zhang, C. Wu, M. Yin, H. Yao, H. Qiu, J. Luo, J. Du and F. Hao, *Adv. Funct. Mater.*, 2024, **34**, 2410772.
11 N. P. Jasti, I. Levine, Y. Feldman, G. Hodes, S. Aharon and D. Cahen, *Proc. Natl. Acad. Sci. U. S. A.*, 2024, **121**, e2316867121.
12 C. C. Stoumpos and M. G. Kanatzidis, *Acc. Chem. Res.*, 2015, **48**, 2791–2802.
13 C. Ortiz-Cervantes, P. Carmona-Monroy and D. Solis-Ibarra, *ChemSusChem*, 2019, **12**, 1560–1575.
14 E. R. Dohner, A. Jaffe, L. R. Bradshaw and H. I. Karunadasa, *J. Am. Chem. Soc.*, 2014, **136**, 13154–13157.
15 H. Tsai, W. Nie, J.-C. Blancon, C. C. Stoumpos, R. Asadpour, B. Harutyunyan, A. J. Neukirch, R. Verduzco, J. J. Crochet, S. Tretiak, L. Pedesseau, J. Even, M. A. Alam, G. Gupta, J. Lou, P. M. Ajayan, M. J. Bedzyk, M. G. Kanatzidis and A. D. Mohite, *Nature*, 2016, **536**, 312–316.
16 J. Hu, L. Yan and W. You, *Adv. Mater.*, 2018, **30**, 1802041.
17 A. Burgos-Caminal, E. Socie, M. E. F. Bouduban and J.-E. Moser, *J. Phys. Chem. Lett.*, 2020, **11**, 7692–7701.
18 L. Mao, W. Ke, L. Pedesseau, Y. Wu, C. Katan, J. Even, M. R. Wasielewski, C. C. Stoumpos and M. G. Kanatzidis, *J. Am. Chem. Soc.*, 2018, **140**, 3775–3783.
19 S. Liu, S. Sun, C. K. Gan, A. G. del Águila, Y. Fang, J. Xing, T. T. H. Do, T. J. White, H. Li, W. Huang and Q. Xiong, *Sci. Adv.*, 2019, **5**, eaav9445.
20 Y. Qin, Z. Lv, S. Chen, W. Li, X. Wu, L. Ye, N. Li and P. Lu, *J. Phys. Chem. C*, 2019, **123**, 22491–22498.
21 T. Yin, B. Liu, J. Yan, Y. Fang, M. Chen, W. K. Chong, S. Jiang, J.-L. Kuo, J. Fang, P. Liang, S. Wei, K. P. Loh, T. C. Sum, T. J. White and Z. X. Shen, *J. Am. Chem. Soc.*, 2019, **141**, 1235–1241.
22 Y. Yuan, X.-F. Liu, X. Ma, X. Wang, X. Li, J. Xiao, X. Li, H.-L. Zhang and L. Wang, *Adv. Sci.*, 2019, **6**, 1900240.
23 Y. Fang, L. Zhang, Y. Yu, X. Yang, K. Wang and B. Zou, *CCS Chem.*, 2020, **3**, 2203–2210.
24 V. Gómez, S. Klyatskaya, O. Fuhr, S. Kalytchuk, R. Zbořil, M. Kappes, S. Lebedkin and M. Ruben, *Inorg. Chem.*, 2020, **59**, 12431–12436.
25 L. Kong, G. Liu, J. Gong, L. Mao, M. Chen, Q. Hu, X. Lü, W. Yang, M. G. Kanatzidis and H.-k. Mao, *Proc. Natl. Acad. Sci. U. S. A.*, 2020, **117**, 16121–16126.
26 H. Li, Y. Qin, B. Shan, Y. Shen, F. Ersan, E. Soignard, C. Ataca and S. Tongay, *Adv. Mater.*, 2020, **32**, 1907364.
27 X. Ren, X. Yan, D. V. Gennep, H. Cheng, L. Wang, Y. Li, Y. Zhao and S. Wang, *Appl. Phys. Lett.*, 2020, **116**, 101901.
28 P. Shen, T. Vogt and Y. Lee, *J. Phys. Chem. Lett.*, 2020, **11**, 4131–4137.
29 C. Tian, Y. Liang, W. Chen, Y. Huang, X. Huang, F. Tian and X. Yang, *Phys. Chem. Chem. Phys.*, 2020, **22**, 1841–1846.
30 R. Fu, W. Zhao, L. Wang, Z. Ma, G. Xiao and B. Zou, *Angew. Chem., Int. Ed.*, 2021, **60**, 10082–10088.
31 F. F. Gao, X. Li, Y. Qin, Z.-G. Li, T.-M. Guo, Z.-Z. Zhang, G.-D. Su, C. Jiang, M. Azeem, W. Li, X. Wu and X.-H. Bu, *Adv. Opt. Mater.*, 2021, **9**, 210003.
32 H. Li, D. Wines, B. Chen, K. Yumigeta, Y. M. Sayyad, J. Kopaszek, S. Yang, C. Ataca, E. H. Sargent and S. Tongay, *ACS Appl. Mater. Interfaces*, 2021, **13**, 44964–44971.
33 L. A. Muscarella, A. Dučinskas, M. Dankl, M. Andrzejewski, N. P. M. Casati, U. Rothlisberger, J. Maier, M. Graetzel, B. Ehrler and J. V. Milić, *Adv. Mater.*, 2022, **34**, 2108720.
34 Y. Fang, J. Wang, L. Zhang, G. Niu, L. Sui, G. Wu, K. Yuan, K. Wang and B. Zou, *Chem. Sci.*, 2023, **14**, 2652–2658.
35 F.-F. Gao, H. Song, Z.-G. Li, Y. Qin, X. Li, Z.-Q. Yao, J.-H. Fan, X. Wu, W. Li and X.-H. Bu, *Angew. Chem., Int. Ed.*, 2023, **62**, e202218675.
36 J. Ratté, M. F. Macintosh, L. DiLoreto, J. Liu, W. Mihalyi-Koch, M. P. Hautzinger, I. A. Guzei, Z. Dong, S. Jin and Y. Song, *J. Phys. Chem. Lett.*, 2023, **14**, 403–412.
37 T. Yin, H. Yan, I. Abdelwahab, Y. Lekina, X. Lü, W. Yang, H. Sun, K. Leng, Y. Cai, Z. X. Shen and K. P. Loh, *Nat. Commun.*, 2023, **14**, 411.
38 F.-F. Gao, Y. Qin, Z.-G. Li, W. Li, J. Hao, X. Li, Y. Liu, C. J. Howard, X. Wu, X. Jiang, Z. Lin, P. Lu and X.-H. Bu, *ACS Nano*, 2024, **18**, 3251–3259.
39 S. Guo, W. Mihalyi-Koch, Y. Mao, X. Li, K. Bu, H. Hong, M. P. Hautzinger, H. Luo, D. Wang, J. Gu, Y. Zhang, D. Zhang, Q. Hu, Y. Ding, W. Yang, Y. Fu, S. Jin and X. Lü, *Nat. Commun.*, 2024, **15**, 3001.
40 M. Mączka, J. A. S. Silva, W. P. Gomes, D. L. M. Vasconcelos, F. Dybała, A. P. Herman, R. Kudrawiec and P. T. C. Freire, *J. Phys. Chem. C*, 2024, **128**, 8698–8707.
41 S. Sobczak, A. Nowok, J. K. Zaręba, K. Roszak, A. Półrolniczak, A. Z. Szeremeta, B. Dziuk, F. Dybała, S. Pawlus, R. Kudrawiec, A. Sieradzki, M. Mączka and A. Katrusiak, *J. Mater. Chem. A*, 2024, **12**, 16803–16814.
42 P. Steeger, M. Adnan, T. Deilmann, X. Li, S. Müller, K. Skrzyńska, M. Hanfland, E. Kolesnikov, J. Kösters, T. Block, R. Schmidt, I. Kupenko, C. Sanchez-Valle, G. V. Prakash, S. M. de Vasconcellos and R. Bratschitsch, *J. Am. Chem. Soc.*, 2024, **146**, 23205–23211.
43 M. Szafrański, *J. Mater. Chem. A*, 2024, **12**, 2391–2399.
44 H. Zhang, P. Zhang, C. Xie, J. Han, B. Xu and Z. Quan, *Adv. Sci.*, 2024, **11**, 2305597.
45 A. Kutty, J. Ratté, R. Guan, J. Liu, S. Tao, Y. Lin, M. P. Hautzinger, W. Mihalyi-Koch, S. Jin and Y. Song, *Adv. Opt. Mater.*, 2025, 2500602.
46 Y. Yin, X. Yan, H. Luo, Y. Liang, P. Xu, Y. Wang, S. Jin and W. Tian, *Angew. Chem., Int. Ed.*, 2025, **64**, e202418587.
47 G. Liu, J. Gong, L. Kong, R. D. Schaller, Q. Hu, Z. Liu, S. Yan, W. Yang, C. C. Stoumpos, M. G. Kanatzidis, H.-k. Mao and T. Xu, *Proc. Natl. Acad. Sci. U. S. A.*, 2018, **115**, 8076–8081.
48 Y. Moritomo and Y. Tokura, *J. Chem. Phys.*, 1994, **101**, 1763–1766.
49 A. Jaffe, Y. Lin and H. I. Karunadasa, *ACS Energy Lett.*, 2017, **2**, 1549–1555.

Open Access Article. Published on 28 Oktober 2025. Downloaded on 16.02.26 09:35:21.
This article is licensed under a Creative Commons Attribution-NonCommercial 3.0 Unported Licence.

50 Y. Chen, R. Fu, L. Wang, Z. Ma, G. Xiao, K. Wang and B. Zou, *J. Mater. Chem. A*, 2019, **7**, 6357–6362.
51 C. Gao, R. Li, Y. Li, R. Wang, M. Wang, Z. Gan, L. Bai, Y. Liu, K. Zhao, S. F. Liu, Y. Cheng and W. Huang, *J. Phys. Chem. Lett.*, 2019, **10**, 5687–5693.
52 L. Zhang, L. Wu, K. Wang and B. Zou, *Adv. Sci.*, 2019, **6**, 1801628.
53 S. Guo, Y. Zhao, K. Bu, Y. Fu, H. Luo, M. Chen, M. P. Hautzinger, Y. Wang, S. Jin, W. Yang and X. Lü, *Angew. Chem., Int. Ed.*, 2020, **59**, 17533–17539.
54 G. Xiang, Y. Wu, M. Zhang, C. Cheng, J. Leng and H. Ma, *Nanomaterials*, 2021, **11**, 2712.
55 M. Mączka, S. Sobczak, P. Ratajczyk, F. F. Leite, W. Paraguassu, F. Dybała, A. P. Herman, R. Kudrawiec and A. Katrusiak, *Chem. Mater.*, 2022, **34**, 7867–7877.
56 M. Mączka, F. Dybała, A. P. Herman, W. Paraguassu, A. J. Barros dos Santos and R. Kudrawiec, *RSC Adv.*, 2024, **14**, 38514–38522.
57 S. Attique, N. Ali, T. Imran, S. Rauf, A. Khesro, S. Ali, W. Wang, R. Khatoon, A. Abbas, E. Ullah khan, S. Yang and H. Wu, *Sol. Energy*, 2022, **239**, 198–220.
58 A. Celeste and F. Capitani, *J. Appl. Phys.*, 2022, **132**, 220903.
59 N. Wang, S. Zhang, S. Wang, X. Yang, F. Guo, Y. Zhang, Z. Gu and Y. Song, *Adv. Funct. Mater.*, 2024, **34**, 2315918.
60 A. Jayaraman, *Rev. Mod. Phys.*, 1983, **55**, 65–108.
61 W. A. Bassett, *High Press. Res.*, 2009, **29**, 163–186.
62 S. Klotz, J. C. Chervin, P. Munsch and G. Le Marchand, *J. Phys. D: Appl. Phys.*, 2009, **42**, 075413.
63 D. Zhaohui and Y. Song, in *Nanowires – Fundamental Research*, ed. H. Abbass, IntechOpen, 2011. vol. 23, pp. 527–552.
64 Z. Dong, *PhD Thesis*, University of Western Ontario, 2012.
65 Z. Dong and Y. Song, *J. Phys. Chem. C*, 2010, **114**, 1782–1788.
66 J. Ratté, *MSc Thesis*, University of Western Ontario, 2022.
67 Y. Xu, T. Gong and J. N. Munday, *Sci. Rep.*, 2015, **5**, 13536.
68 K. Wang, L. Zheng, Y. Hou, A. Nozariasbmarz, B. Poudel, J. Yoon, T. Ye, D. Yang, A. V. Pogrebnyakov, V. Gopalan and S. Priya, *Joule*, 2022, **6**, 756–771.
69 M. Pitaro, E. K. Tekelenburg, S. Shao and M. A. Loi, *Adv. Mater.*, 2022, **34**, 2105844.
70 A. Filippetti, S. Kahmann, C. Caddeo, A. Mattoni, M. Saba, A. Bosin and M. A. Loi, *J. Mater. Chem. A*, 2021, **9**, 11812–11826.
71 C. C. Stoumpos, C. D. Malliakas and M. G. Kanatzidis, *Inorg. Chem.*, 2013, **52**, 9019–9038.
72 H.-H. Fang, S. Adjokatse, S. Shao, J. Even and M. A. Loi, *Nat. Commun.*, 2018, **9**, 243.
73 M. Morana and L. Malavasi, *Sol. RRL*, 2021, **5**, 2100550.
74 M. Konstantakou and T. Stergiopoulos, *J. Mater. Chem. A*, 2017, **5**, 11518–11549.
75 L. Kong, J. Gong, I. Spanopoulos, S. Yan, Z. Li, Z. Zhu, X. Liu, Y. Zhu, H. Dong, H. Shu, Q. Hu, W. Yang, H.-k. Mao, M. G. Kanatzidis and G. Liu, *Adv. Funct. Mater.*, 2024, **34**, 2414437.
76 Y. Li, Z. Zhou, N. Tewari, M. Ng, P. Geng, D. Chen, P. K. Ko, M. Qammar, L. Guo and J. E. Halpert, *Mater. Chem. Front.*, 2021, **5**, 4796–4820.
77 J. Wen, K. Rong, L. Jiang, C. Wen, B. Wu, B. Sa, Y. Qiu and R. Ahuja, *Nano Energy*, 2024, **128**, 109802.
78 S. Dutta, S. K. D. Vishnu, S. Som, R. Chaurasiya, D. K. Patel, K. Moovendaran, C.-C. Lin, C.-W. Chen and R. Sankar, *ACS Appl. Electron. Mater.*, 2022, **4**, 521–530.
79 X. Zhan, X. Jiang, P. Lv, J. Xu, F. Li, Z. Chen and X. Liu, *Angew. Chem., Int. Ed.*, 2022, **61**, e202205491.
80 A. Jaffe, S. A. Mack, Y. Lin, W. L. Mao, J. B. Neaton and H. I. Karunadasa, *Angew. Chem., Int. Ed.*, 2020, **59**, 4017–4022.
81 Q. Li, S. Li, K. Wang, Z. Quan, Y. Meng and B. Zou, *J. Phys. Chem. Lett.*, 2017, **8**, 500–506.
82 Y. Zhou, D. Zhao, F. Wang, Y. Shi, Z. Ma, R. Fu, K. Wang, Y. Sui, Q. Dong, G. Xiao and B. Zou, *Phys. Rev. Mater.*, 2023, **7**, 074002.
83 R. Chiara, M. Morana and L. Malavasi, *ChemPlusChem*, 2021, **86**, 879–888.
84 M. Morana, R. Chiara, B. Joseph, T. B. Shiell, T. A. Strobel, M. Coduri, G. Accorsi, A. Tuissi, A. Simbula, F. Pitzalis, A. Mura, G. Bongiovanni and L. Malavasi, *iScience*, 2022, **25**, 104057.
85 Q. Li, L. Yin, Z. Chen, K. Deng, S. Luo, B. Zou, Z. Wang, J. Tang and Z. Quan, *Inorg. Chem.*, 2019, **58**, 1621–1626.
86 J. Zhang, M. Li, D. Wang, B. Chu, S. Zhang, Q. Xu and K. Wang, *J. Mater. Chem. A*, 2023, **11**, 19427–19434.

 This journal is © The Royal Society of Chemistry 2026